Submitted, J.N.N.F.M., July 19, 2000.

THE AXISYMMETRIC CONTRACTION-EXPANSION: THE ROLE OF EXTENSIONAL RHEOLOGY ON VORTEX GROWTH DYNAMICS AND THE ENHANCED PRESSURE DROP

Jonathan P. Rothstein and Gareth H. McKinley
Dept. of Mechanical Engineering, Massachusetts Institute of Technology
Cambridge, MA 02139; USA

Abstract

The flow of a polystyrene Boger fluid through axisymmetric contraction-expansions having various contraction ratios ($2 \# b \# 8$) and degrees of re-entrant corner curvatures are studied experimentally over a large range of Deborah numbers. The ideal elastic fluid is dilute, monodisperse and well characterized in both shear and transient uniaxial extension. A large enhanced pressure drop above that of a Newtonian fluid is observed independent of contraction ratio and re-entrant corner curvature. Streak images, laser Doppler velocimetry and digital particle image velocimetry are used to investigate the flow kinematics upstream of the contraction plane. LDV is used to measure velocity fluctuation in the mean flow field and to characterize a global elastic flow instability which occurs at large Deborah numbers. For a contraction ratio of $b = 2$ a steady elastic lip vortex is observed while for contraction ratios of $4 \# b \# 8$ no lip vortex is observed and a corner vortex is seen. Rounding the re-entrant corner leads to shifts in the onset of the flow transitions at larger Deborah numbers, but does not qualitatively change the overall structure of the flow field. We describe a simple rescaling of the deformation rate which incorporates the effects of lip curvature and allows measurements of vortex size, enhanced pressure drop and critical Deborah number for the onset of elastic instability to be collapsed onto master curves. Transient extensional rheology measurements are utilized to explain the significant differences in vortex growth pathways (i.e. elastic corner vortex versus lip vortex growth) observed between the polystyrene Boger fluids used in this research and polyisobutylene and polyacrylamide Boger fluids used in previous contraction flow experiments. We show that the role of contraction ratio on vortex growth dynamics can be rationalized by considering the dimensionless ratio of the elastic normal stress difference in steady shear flow to those in transient uniaxial extension. It appears that the differences in this normal stress ratio for different fluids at a given Deborah number arise from variations in solvent quality or excluded volume effects.

Keywords: axisymmetric contraction-expansion, entrance pressure drop, dissipative stress, polystyrene Boger fluid, PIV, LDV, vortex growth dynamics, entrance lip singularity, extensional rheology

1. Introduction

The flow of a viscoelastic fluid through an axisymmetric contraction-expansion is a complex flow containing regions of strong shearing near the walls, nonhomogeneous uniaxial extension along the centerline upstream of the contraction plane and nonhomogeneous biaxial expansion downstream of the expansion. The contraction flow is a long-standing numerical benchmark for computation of non-Newtonian fluids [1; 2] and is the subject of several excellent review articles [3; 4]. The present paper, in conjunction with our previous work focusing on the 4:1:4 axisymmetric abrupt contraction-expansion [5], is intended to constitute a comprehensive set of quantitative experimental measurements to which theory and numerical simulations can be rigorously compared. To meet this goal, an ideal monodisperse, dilute Boger fluid is first thoroughly characterized in both shear and extension. This ideal elastic fluid is then used to investigate the kinematics of the flow through several axisymmetric contraction-expansions of different contraction ratios and varying lip curvatures over a wide range of Deborah numbers. The experimental measurements include global pressure drop and local velocity measurements as well as streak images of the elastically-enhanced upstream vortex structures.

Experimental measurements of the pressure drop for polymer solutions flowing through abrupt axisymmetric contraction-expansions have shown a substantial extra pressure drop well above the value observed for a Newtonian fluid with equal viscosity at the same flow rates [5; 6]. In neither case was the observed viscoelastic enhancement of the pressure drop associated with the onset of an elastic or an inertial flow instability; however, it is not even qualitatively predicted by existing steady-state or transient numerical computations with simple dumbbell models [7-9]. In fact, these models predict a significant viscoelastic *decrease* in the pressure drop with addition of polymer to a Newtonian solvent. The failure of these

constitutive models to predict the correct evolution in the properties of complex flows with Deborah number may be due to an inadequate description of the internal molecular conformations of the polymer chains that arise during rapid stretching. This is evident in measurements of transient uniaxial extension where the existence of a *stress-conformation-hysteresis* has been experimentally observed [10; 11] and computed in bead-rod and bead-spring computations [10; 12] but has yet to be quantitatively predicted by any simple closed-form differential constitutive model. A complete discussion of previous experimental and numerical studies involving pressure drop measurements in contraction flows can be found in Rothstein and McKinley [5]. One of the major goals of the present study is to determine what effects systematic changes in the contraction ratio and the curvature of the re-entrant corner will have on the magnitude and the onset of this enhanced pressure drop. Investigation of the role of lip curvature is especially important because a major computational impediment to simulations of the viscoelastic flow through a contraction-expansion is the development of singular stress fields near a sharp re-entrant corner.

Measurements of the evolution in the pressure drop generate information about the global state of viscoelastic stress in the flow and are an excellent comparative tool when utilized in conjunction with measurements of the flow kinematics such as streak images and velocity measurements. There have been a great number of experimental investigations dealing with the kinematics of the flow through a contraction over a wide range of Deborah numbers, contraction ratios and re-entrant corner curvatures using a large variety of different viscoelastic fluids [3; 4; 13]. In experiments with elastic polymer solutions two distinct pathways for evolution of the vortex growth with Deborah number have been observed, which lead to flow structures typically described in the literature as corner and lip vortices. In each case, a weak, Newtonian 'Moffatt eddy' is present in the upstream stagnant corner at low Deborah numbers. In the regime of corner

vortex growth, the upstream vortex near the stagnant corner increases in strength and grows radially inward. Upon reaching the re-entrant corner, the vortex proceeds to grow steadily upstream with increasing Deborah number. This pathway can be accurately captured by simulations with appropriate viscoelastic constitutive models [8; 14]. By contrast, the lip vortex growth regime is characterized by a decrease in the corner vortex size as the Deborah number is increased and the formation of a separate, distinct elastically-dominated 'lip' vortex near the re-entrant corner [15]. The vortex spreads radially outward toward the stagnant corner and subsequently grows upstream in a manner quite similar to the corner vortex growth described above. At very high Deborah numbers, the large upstream vortex observed for both of the vortex growth patterns becomes unstable to a global dynamical mode that is a sensitive, non-monotonic function of the contraction ratio [16; 17].

The sequence of flow patterns chosen by the viscoelastic fluid is a complex function of the contraction ratio and the re-entrant lip curvature. Results prior to 1987 are summarized in Boger [3] and Table 1 summarizes more recent observations for several different Boger fluid formulations. In general, as the contraction ratio is increased, the flow moves from the lip vortex to the corner vortex flow regime, but the critical contraction ratio for this crossover in vortex evolution pathway is strongly dependent on the properties of the test fluid and impossible to predict *a priori*. So, why do two elastic fluids such as PIB/PB and PAA/CS Boger fluids, which have very similar viscoelastic properties, act so differently in this and other complex flows? Many researchers have postulated that the answer must arise from differences in the transient extensional rheology [5; 13; 16; 18]. Until quite recently, reliable measurements of the extensional stress of dilute polymer solutions undergoing ideal uniaxial extension were not possible, but with the advent of the filament stretching rheometer, transient uniaxial extensional rheology measurements are now attainable

[19], making it possible to test the validity of such assertions.

	Sharp Re-Entrant Corner		Rounded Re-Entrant Corner	
Boger Fluid	Corner Vortex	Lip Vortex	Corner Vortex	Lip Vortex
PIB/PB [13; 16]	$b \geq 8$	$2 \leq b \leq 6.8$	$b \geq 8$	$2 \leq b \leq 6.8$
PAA/CS [3; 13; 20]	$b \geq 4$	$b \leq 2$	$b > 4$	$b \leq 4$
PS/PS [5]	$b = 4$			

Table 1: Vortex growth dynamics for several Boger fluids at various contraction ratios ($b = R_1/R_2$, where R_1 is the upstream radius and R_2 is the radius of the contraction) and re-entrant corner radii of curvature.

The effect of lip curvature on the vortex growth dynamics is also summarized in Table 1. Boger and Binnington [13] presented a systematic photographic study using PIB/PB and PAA/CS Boger fluids while the vortex growth dynamics observed using a similar PIB/PB Boger fluid were discussed by McKinley et al. [16]. These previous studies show that, for the PIB/PB Boger fluid at the contraction ratios examined, rounding the re-entrant corner leads to increases in the critical Deborah numbers for flow transitions, but does not qualitatively change the kinematics of the flow field. However, rounding the re-entrant corner of the 4:1 contraction with a radius of curvature equal to 36% of the contraction radius ($R_c = 0.36R_2$) results in a dramatic change in the vortex evolution for the PAA/CS solution [13]. Streak images recorded upstream of the sharp re-entrant corner, clearly demonstrate the growth dynamics of a corner vortex. However, the nature of the contraction flow was completely changed by rounding the re-entrant corner. The formation of the expected corner vortex is suppressed and supplanted by a lip vortex [13]. Boger and Binnington thus argue that the evidence suggests that rounding the re-entrant corner is equivalent to decreasing the contraction ratio.

In addition to investigating the evolution of the pressure drop, another goal of the present study is

to determine which vortex evolution path is followed by a dilute and monodisperse polystyrene Boger fluid that has been well characterized in both extension and in steady and transient shear flows. To date, we have reported measurements for flow through a 4:1:4 contraction-expansion, but a detailed analysis of the effect of contraction ratio and re-entrant corner radii of curvature will generate additional insight into the trends observed in the published data on PIB/PB and PAA/CS Boger fluids listed in Table 1 when analyzed in conjunction with measurements of the transient extensional rheology.

We describe our experimental apparatus and techniques in §2 and report both the steady shear and transient uniaxial extensional rheology of the fluid. In §3, we first present observation of the enhanced pressure drop through several different contraction-expansions. Flow visualization, digital particle image velocimetry (DPIV) and laser Doppler velocimetry (LDV) are then combined to characterize the evolution in the kinematics of the fluid motion with increasing Deborah number. LDV measurements of fluctuations in the fluid velocity are then used to document the onset of an elastic instability that eventually leads to global oscillations in the flow and the development of an interesting jetting instability as the Deborah number is increased. Finally, in §4 we discuss the implications of our findings for simulation and modeling of elastic flows through contractions.

2. Experimental

2.1. Flow geometry

A schematic diagram of the axisymmetric contraction-expansion and the important length scales associated with it is shown in Figure 1. The radii of the cylindrical tubes upstream and downstream of the contraction-expansion are equal and remain constant at R_1 (=1.27cm) while the radius within the throat of the contraction is given by R_2. Several different orifice plate configurations yielding various contraction

ratios ($ß$ / R_1 / R_2), contraction lengths (L_c) and re-entrant corner radii of curvature (R_c) are used in this study and are listed in dimensionless form in Table 2.

Description	Contraction Ratio ($ß$ / R_1 / R_2)	Re-entrant Lip Curvature (R_c / R_2)	Contraction Length (L_c / R_2)
2:1:2	2	< 0.01	0.5
4:1:4	4	< 0.01	1
4:1:4 Rounded	4	0.5 upstream only	1
8:1:8	8	< 0.01	2
8:1:8 Rounded	8	0.18 upstream and downstream	2

Table 2: Description of orifice plate geometries used in this study. In each case the value of the upstream radius is R_1 = 1.3cm.

In order to quantify the upstream vortex growth dynamics, it is necessary to define several dimensionless length scales to describe both the size and position of the vortex: the distance to the separation point (? / L_v/R_2) and the coordinates of the center of the recirculation denoted by the distance from the contraction plane (? / Z_v / R_2) and from the centerline (? / R_v / R_2).

As described in Rothstein and McKinley [5], the fluid is forced at a constant volume flow rate, Q, past two flush mounted pressure transduces, here denoted P_u and P_d, located at positions z_u = !7.62cm far upstream and z_d = 8.26cm far downstream of the contraction plane (located at z = 0). Under steady flow conditions, the pressure difference measured between the upstream and downstream transducers results from a combination of the pressure drop due to Poiseuille flow in the tube and an extra pressure drop caused by the presence of the contraction-expansion, $?P_{ud} = P_u ! P_d = ?P_{Poiseuille} + ?P_{extra}$. To isolate the extra pressure drop across the contraction-expansion, the pressure drop resulting from the Poiseuille flow in the upstream and downstream tubing as

well as the Poiseuille flow within the throat of the contraction-expansion are removed

$$\Delta P'_{ud} = \Delta P_{ud} - \frac{8Qh}{\pi}\left(\frac{L}{R_1^4} + \frac{L_c}{R_2^4}\right), \qquad \textbf{(1)}$$

where L / (z_u ! z_d) ! L_c is the total length of straight pipe of radius R_1 between the pressure transducers and ? is the viscosity of the fluid. When the re-entrant corner of the contraction-expansion is rounded, the flow within the throat is no longer Poiseuille-like over the entire contraction length. An approximate numerical solution to the flow past the rounded re-entrant corner can be calculated for creeping flow of a Newtonian fluid using lubrication theory or alternatively the exact value could be computed numerically; however, for simplicity of presentation, the pressure drop resulting from the Poiseuille flow over the entire contraction length (L_c) is removed from the experimental pressure drop measurements irrespective of the degree of re-entrant lip curvature. Finally, we define a dimensionless pressure drop

$$P\left(De, R_c, b\right) = \frac{\Delta P'_{ud}\left(Q, De, R_c, b\right)}{\Delta P'_{ud}\left(Q, De = 0, R_c = 0, b = 4\right)}, \qquad \textbf{(2)}$$

where the pressure drop resulting from the flow of a Newtonian fluid across a 4:1:4 sharp axisymmetric contraction-expansion at a given flow rate, ? P_{ud} (Q, De = 0, R_c = 0, b = 0), is used in the denominator to non-dimensionalize the pressure drop resulting from the flow of the non-Newtonian test fluid across each of the contraction-expansions at the same flow rate, regardless of aspect ratio and re-entrant lip curvature.

2.2. Measurement Techniques

The flow field upstream of the axisymmetric abrupt contraction is investigated using several different techniques: digital particle image velocimetry (DPIV); laser Doppler velocimetry (LDV); and flow visualization through computer-generated streak images. A complete discussion of the DPIV and flow

visualization techniques used in this paper can be found in Rothstein and McKinley [5].

In the present study, LDV measurements are used to supplement the global velocity vector field measurements obtained with DPIV. Primarily, we utilize LDV to take pointwise measurements of velocities near and within the throat of the contraction-expansion where DPIV measurements are not possible due to the loss of cross-correlation between sequential images in subregions where the velocity or velocity gradient of the particles become too large. To facilitate these measurements, an acrylic 4:1:4 orifice plate was created to form the contraction-expansion. LDV can generate time-resolved point velocity measurements which can be used to search for the onset of elastic flow instabilities near the contraction plane [15]. The test fluid is seeded with the same 50μm diameter silvered hollow glass spheres (Potters Industry) used for DPIV and flow visualization purposes [5]. Utilizing a fast Fourier transform technique, a spectrum analyzer (Dantec Burst Spectrum Analyzer) is used to compute the velocity from the Doppler shifted frequency signal collected from a single-colored, fiber optic LDV system (Dantec Electronics Inc.) coupled with a 300mW argon-ion laser (Ion Laser Technologies). A detailed description of the LDV system used in this research is presented by Arigo et al. [21]. The spectrum analyzer is an excellent tool for extracting average velocities from ensembles of Doppler bursts for slow flows, even in the presence of noise, but because of the discrete nature and random arrival times of the Doppler bursts, spectral analysis cannot always be used to effectively resolve slow time-varying velocity profiles such as those that develop beyond the onset of flow instabilities. A Doppler frequency tracker (DISA, Model 55 N 21) is therefore used to lock into and measure the frequency and amplitude of velocity fluctuations resulting from elastic flow instabilities. These local velocity measurements are a more sensitive indicator of the critical conditions for the onset of the elastic flow instability than the global measurements of the pressure drop used in our

previous study [5].

2.3. Fluid Rheology

The viscoelastic test fluid used in these experiments consists of an 0.025 wt% solution of monodisperse polystyrene (PS) (Scientific Polymer Products, Inc.) with a molecular weight of 2.25×10^6 g/mol and polydispersity of 1.03 dissolved in oligomeric styrene (Hercules). The solution is a dilute Boger fluid with $c/c^* = 0.24$ [22]. For completeness, a master curve of the rheological properties for the 0.025% PS/PS solution at T_0 = 25EC, measured with a controlled stress device (TA Instruments, Model AR1000N), is reproduced in Figure 2 [5]. The viscoelastic properties of the fluid are characterized in small amplitude oscillatory shear flow by the dynamic viscosity ?N(?) and the dynamic rigidity 2?O(?)/? while in steady shear flow, the fluid is characterized by the first normal stress coefficient ? 1(?)= (t_{11}(?)! t_{22}(?))/?2 and viscosity ?(?). The use of the Rouse-Zimm [23] and the FENE-P model [24] fits plotted in Figure 2 have been discussed in great detail in Rothstein and McKinley [5]. Table 3 contains the parameters describing the viscometric properties of the PS/PS solution. As shown in Figure 2, the viscosity of the solution is approximately constant over several decades of shear rate. The fluid is strongly elastic and the first normal stress coefficient shear-thins monotonically throughout the entire range over which data can be obtained. By contrast, the Rouse-Zimm bead-spring model predicts a constant value of the first normal stress coefficient as a consequence of the pre-averaging of hydrodynamic interactions [25]. The dash-dotted lines in Figure 2 represent the predictions of the FENE-P model for the steady shear data. The value of the finite extensibility parameter, L^2, used in the FENE-P model is computed from molecular quantities rather than from fitting and clearly leads to an overprediction of the viscometric properties. An improved description requires a more detailed treatment of hydrodynamic interactions between segments

of a polymer chain undergoing a steady shearing deformation. One such model that accounts for the anisotropy in the hydrodynamic drag forces in approximate form is the encapsulated dumbbell model of Bird and DeAguiar [26]. The evolution equations of the Bird-DeAguiar model can be re-written as

$$l\,\mathbf{A}_{(1)} = -\left[f\left(tr\mathbf{A}\right)\mathbf{A} - \mathbf{I} \right] + 3\left(1 - sb\right)\frac{\mathbf{A}}{tr\mathbf{A}} - \left(1 - sb\right)\mathbf{I}, \tag{3}$$

$$\mathrm{t}_{p} = -n\mathrm{k}_{\mathrm{B}}T\left[f\left(tr\mathbf{A}\right)\mathbf{A} - \mathbf{I} \right] + 2n\mathrm{k}_{\mathrm{B}}T\left(1 - b\right)\left[\frac{3\mathbf{A}}{tr\mathbf{A}} - \mathbf{I} \right], \tag{4}$$

$$\text{where} \quad f\left(tr\mathbf{A}\right) = \frac{1}{1 - \dfrac{tr\mathbf{A}}{L^{2}}}, \tag{5}$$

where k_{B} is the Boltzman constant, n is the number of springs, l is the relaxation time of the fluid, L is the finite extensibility of the polymer chain and the polymer conformation is given by the dimensionless second moment tensor $\mathbf{A} = \langle \mathbf{RR} \rangle$, where $\mathbf{R}$ is the end-to-end vector of the polymer chain scaled with the root mean square end-to-end length of the chain. The extent of anisotropy in the viscous drag on the beads is given by s and the anisotropy in the velocity distribution of the beads arising from Brownian motion is given by $ß$. When $s = ß = 1$, the FENE-P model is recovered. Our exploratory calculations suggest that to quantitatively describe the viscometric properties of dilute polymer solutions in viscous solvents, the anisotropy in the viscous drag the primary effect of importance. The Brownian motion of the beads can thus be assumed to be isotropic with $ß = 1$. In this limit, Equation 4 reduces to the familiar expression for the stress in an ensemble of FENE-P dumbells while the evolution equation reduces to

$$l\ \mathbf{A}_{(1)} = -\left[\left\{ f\ (tr\,\mathbf{A}\ ) - \frac{3\,(1 - s\ )}{tr\,\mathbf{A}} \right\} \mathbf{A} - s\ \mathbf{I} \right], \tag{6}$$

The solid lines in Figure 2 represent the predictions of the Bird-DeAguiar model fit and are in good agreement with both the viscosity and first normal stress difference measurements.

	Notation	Description	Parameter
Known:	c	Concentration of High Molecular Weight Polystyrene	0.025%
	M_w ' M_n	Polydispersity	1.03
	M_w	Molecular Weight [g/mol]	2.0×10^6
	$b = L^2$	Extensibility Parameter	26900
	T_0	Reference Temperature [K]	298
Fitted:	$?_0$	Zero Shear Rate Viscosity [Pa•s]	22.75
	$?_s$	Solvent Viscosity [Pa•s]	21
	$?_{ps}$	Solvent Relaxation Time [s]	2.5×10^{-4}
	h*	Hydrodynamic Interaction Parameter	0.1
	s	Extent of Anisotropy in Stokes' Law	0.63
	ß	Extent of Anisotropy in Brownian Motion Forces	1
Calculated:	$?_z$	Zimm (Longest) Relaxation Time [s]	3.24
	$\overline{?}$	Oldroyd Relaxation Time [s]	0.146
	$?_{10}$	First Normal Stress Coefficient [Pa•s^2]	6.66

Table 3: Parameters characterizing the viscometric properties of the 0.025wt% PS/PS solution.

To understand the kinematics of the complex flow through axisymmetric contraction-expansions, it is important to characterize the behavior of the test fluid in both shear and extension. The filament stretching rheometer and techniques developed by Anna et al. [27] were used to measure the transient extensional viscosity of the PS/PS solution. In Figure 3, the Trouton ratio, $Tr = \bar{h}^+ / h_0$, is plotted against the Hencky strain, $e = \dot{e}t$, for a strain rate of $\dot{e} = 9.1\text{s}^{-1}$. One important point to note is that at high Deborah numbers, $De = l_z\dot{e} = 29.5$, the Trouton ratio is relatively insensitive to changes in extension rate. At low

Hencky strains, the extensional viscosity behaves in a Newtonian-like manner and the Trouton ratio is approximately equal to $Tr = 3\eta_s / \eta_0$. As the Hencky strain increases, the PS/PS solution strain-hardens, reaching an equilibrium at a Trouton ratio of $Tr \sim 1000$. The FENE-P and Bird-DeAguiar model fits are plotted with the experimental data. Neither of these models fit the experimental data well, overpredicting the critical Hencky strain for the onset of strain-hardening and overpredicting the equilibrium value of the extensional viscosity. It is interesting to note that the anisotropy introduced by the Bird-DeAguiar model has very limited effect in uniaxial extension even though it has a profound effect on the prediction of the first normal stress differences in shear.

2.4. Dimensionless Parameters

In this research, the characteristic Reynolds number based on the flow conditions at the contraction plane is given by $Re = 2\rho \bar{v}_{z,2} R_2 / \eta_0$, where $\bar{v}_{z,2} = Q / \pi R_2^2$ is the average axial velocity in the throat of the contraction, Q is the volume flow rate and $\rho = 1.026$ g/cm^3 is the density of the fluid. For all the experiments performed the Reynolds number is $Re < 1\times10^{-2}$, thus inertial effects are negligible.

The Deborah number, $De = \lambda/T$, characterizes the relative importance of elastic effects to viscous effects in the flow. To determine the Deborah number a characteristic flow timescale, T, and a characteristic relaxation time of the fluid, λ, must be selected. The characteristic convective timescale of the flow can then be taken to be the inverse of the deformation rate in the vicinity of the throat of the contraction plane, $T \sim R_2 / \bar{v}_{z,2} = \dot{\gamma}^{-1}$. The choice of the appropriate relaxation time of the fluid is discussed in depth in Rothstein and McKinley [5]. This work will follow the same convention, choosing the zero-shear-rate relaxation time, $\lambda_0 = \lambda_{10} / 2\eta_0$. Thus, the Deborah number used in presentation of the

results of this research is given by $De = ?_0 + v_{z,2} / R_2$. As we show in §4, the qualitative effects of lip curvature can also be incorporated by a single reconsideration of the residence time of the fluid element near the contraction plane.

3. Results

3.1. Pressure Drop Measurements

The evolution in the total pressure drop ($? P_{ud}$) of the 0.025% PS/PS solution flowing through the four contraction-expansion geometries described in §2.1 was measured for Deborah numbers De #10.5. In our previous study [5], it was shown that the Stokes flow solution provided by Sampson for the pressure drop through an infinitesimally thin circular hole in an unbounded rigid wall [28] was in good agreement with the pressure drop measurements for the flow of the Newtonian oligomeric polystyrene into a 4:1:4 contraction-expansion (corrected using Equation 1)

$$\Delta P'_{ud}\left(Q, De = 0, R_c = 0, b = 4\right) \cong \Delta P_{Sampson} = \frac{3h_0 Q}{R_2^3}, \qquad \textbf{(7)}$$

and this value was thus used to generate the dimensionless pressure drop defined in Equation 2.

3.1.1. Effect of Contraction Ratio

The effect of contraction ratio on the dimensionless extra pressure drop is shown in Figure 4. In the absence of elasticity, the pressure drop across the various contraction-expansions should be equal to that of a Newtonian fluid. In other words, in the limit $De \to 0$ we expect $P \to (ß / 4)^3$. This is true for both the 4:1:4 and 8:1:8 contraction-expansion, however, for a contraction ratio of $ß = 2$, the Sampson flow assumption of upstream and downstream fluid reservoirs with infinite lateral extent is no longer a good approximation. The presence of the upstream and downstream walls result in a dimensionless pressure

drop considerably smaller than expected, $P(De << 1, \beta = 2) \approx 0.08$. As the Deborah number is increased, the measurements for each of the contraction ratios examined show a monotonic increase in the dimensionless pressure drop beginning at a critical Deborah number. The value of the critical Deborah number increases slightly with contraction ratio, $0.3 \approx De_{crit} \approx 0.8$, but is consistently close to the Deborah number at which the *coil-stretch transition* occurs in a homogeneous extensional flow, $De = 0.5$. As the Deborah number is increased still further the rate of increase in the dimensionless pressure drop is greatly reduced. These trends in the evolution of the entrance pressure drop have been observed previously in experimental studies of polyacrylamide-based [6] and polystyrene-based fluids flowing [5] through 4:1:4 axisymmetric contraction-expansions, the latter being reproduced in Figure 4. As stated previously, these large additional pressure drops associated with the addition of very small amounts of high molecular weight polymers to Newtonian solvents have yet to be even qualitatively simulated numerically [7-9].

The onset of an elastic flow instability is also indicated in the pressure drop data in Figure 4. A complete discussion of the nature of this elastic flow instability is presented in §3.4. A hypothetical sketch of the line of neutral stability motivated by previous studies of PIB/PB fluids [16] is superimposed over the 4:1:4 and 8:1:8 data. Limitations in the hardware and the sensitivity of our measurement techniques made it impossible to reach Deborah numbers large enough to observe an elastic instability in the 2:1:2 contraction-expansion. It is important to note that, in each case, the enhanced pressure drops measured experimentally are not directly connected with the onset of any elastic instabilities. Thus, regardless of whether a numerical simulation can predict the onset of an elastic instability, the constitutive model should still be able to predict the large enhanced pressure drops associated with steady viscoelastic entrance flow

before any flow instabilities occur.

3.1.2. Effect of Re-entrant Corner Curvature

The effect of re-entrant corner curvature on the dimensionless pressure drop is shown in Figure 5 for the 4:1:4 contraction-expansion with sharp ($R_c < 0.01R_2$) and rounded ($R_c = 0.5R_2$) re-entrant corners. The resulting plots are very similar to Figure 4, showing all the same qualitative features. At low Deborah numbers, the dimensionless pressure drop is Newtonian-like for both re-entrant corner curvatures. The limiting value of the dimensionless pressure drop at low Deborah number for the rounded re-entrant corner is small, $\Pi \approx 0.35$, because the presence of the re-entrant corner curvature has essentially been ignored in Equations 4 and 5. The regions of strong enhanced pressure drop and the onset of the elastic instability are still present even when the re-entrant corner has been rounded. In fact, the only noticeable effect is a shift of onset conditions for different flow regimes to higher Deborah numbers with increasing re-entrant corner curvature. This is consistent with an overprediction of the characteristic deformation rate near the throat, which is at present taken to be the deformation rate within the contraction throat, $\dot{\gamma} = +v_{z,2} / R_2$, independent of re-entrant corner curvature. We return to this shift in onset conditions in §4.

These experiments show that the existence of enhanced pressure drop measurements above and beyond the Newtonian pressure drop ($\Pi > 1$) do not depend qualitatively on re-entrant corner curvature nor on the onset of elastic instabilities. Thus, numerical simulations should be able to remove the singularity associated with the sharp re-entrant corner and without hindering the ability of the constitutive model to predict the large enhanced pressure drop seen in experiments.

3.2. Vortex Growth Dynamics

Flow visualization was used to observe the vortex growth dynamics upstream of the contraction for the four geometries describe in §2.2 for Deborah numbers *De* . 11. A detailed description of the vortex growth and development in the 4:1:4 contraction-expansion with increasing Deborah number has been presented in Rothstein and McKinley [5] and here we focus on changes resulting from varying the lip curvature and the contraction ratio.

3.2.1. Effect of Re-entrant Corner Curvature

The pseudo-streak images on the left-hand side of Figure 6 show the vortex growth and development of the vortex upstream of the sharp 4:1:4 contraction-expansion at Deborah numbers of *De* = 1.6, 2.6 and 3.6 while the images on the right-hand side show the vortex development upstream of the 4:1:4 rounded contraction-expansion at the same Deborah numbers. These images demonstrate the dramatic delay in corner vortex development that results from the introduction of curvature to the re-entrant corner. At low Deborah numbers the PS/PS solution is essentially Newtonian and small, weak recirculation zones known as 'Moffatt vortices', which characteristically have concave dividing streamlines, exist in the stagnant corners just upstream of the contraction plane. An example of the flow patterns observed before the vortex growth and the increase in the pressure drop is shown in Figure 6(d). As the Deborah number is increased, the corner vortices increase in size and strength, Figure 6(a) and 6(e). The corner vortex 'fingers' out towards the contraction entrance and the dividing streamline becomes convex. As the Deborah number is increased still further, a pronounced increase in the dimensionless pressure drop is observed and the corner vortex begins to grow upstream, Figure 6(b) and 6(f). In Figure 6(c), the presence of a global instability in the flow is evident from the non-symmetric corner vortex. Visual observations and LDV measurements of this vortex show that the vortex boundary precesses in the

azimuthal direction so that fluid elements in fact follow a helical path into the orifice.

The vortex growth dynamics of the 4:1:4 rounded contraction-expansion are quantified in Figure 7 through measurements of the dimensionless reattachment length and coordinates of the vortex center as a function of Deborah number. To motivate the discussion of re-entrant corner curvature effects, the reattachment length of the 4:1:4 sharp contraction-expansion has been superimposed over the complete set of 4:1:4 rounded contraction-expansion data. At low Deborah numbers, the dimensionless reattachment length is constant with the expected value for creeping Newtonian flow. As the flow rate is increased, the reattachment length and the axial location of the vortex center begin to increase monotonically with Deborah number. The radial location of the vortex center moves inward from the stagnant corner to a position *?* - 2 which then remains constant as the vortex grows upstream with increasing Deborah number. Upon the onset of the elastic flow instability, all of the measured lengths begin to oscillate with the unsteady motion of the vortex. These data show the same general functional dependence on Deborah number as our earlier measurements for the sharp 4:1:4 contraction-expansion [5]. The principal result of rounding of the re-entrant corner is to cause a delay of the vortex growth dynamics to higher Deborah number.

3.2.2. Effect of Contraction Ratio

In Figure 8, the dimensionless reattachment length and coordinates of the vortex center are shown for the 8:1:8 contraction-expansion. The vortex growth dynamics for the 8:1:8 contraction expansion are similar to those described above; dominated by the presence and upstream growth of an elastic corner vortex. The principal difference arises from the onset conditions for the transitions into different vortex growth regimes. For both the 4:1:4 and the 8:1:8 contraction-expansions the critical Deborah number for the onset of observable corner vortex growth is approximately 20% larger than that for the onset of

enhanced pressure drop growth. The kinematics of these two effects appear to be quite strongly correlated.

In Figure 9, pseudo streak images upstream of the 2:1:2 contraction-expansion are shown for Deborah numbers of De = 0.6, 0.9, 1.1 and 1.5. As observed for both the 4:1:4 and the 8:1:8 contraction-expansions, at low Deborah numbers a Moffatt vortex is present in the upstream stagnant corner as shown in Figure 9(a). However, in contrast to the results presented for the previous contraction ratios, as the Deborah number approaches unity, the corner vortex decreases in size and a separate and distinct 'lip' vortex forms near the re-entrant corner, Figure 9(b). The lip vortex then proceeds to grow outward, Figure 9(c), until it reaches the stagnant corner at which point it grows upstream in a manner consistent with the corner vortex growth dynamics described above for larger contraction ratios.

Digital particle image velocimetry (DPIV) measurements for Deborah numbers of De = 0.9 and 1.5 are shown in Figure 10. These velocity vector field measurements correspond to the streak images shown in Figures 9(b) and 9(c). The vectors are scaled such that an arrow of length $l / R_2 = 0.25$ corresponds to a velocity magnitude of $v / \langle v_z \rangle_2 = 1$. The DPIV measurements in Figure 10(a) demonstrate the complete suppression of the corner vortex with the presence of the lip vortex. In fact, the fluid flows into the stagnant corner and then reverses direction in order to flow back upstream, around the lip vortex and into the contraction. The vector field in Figure 10(b) is very similar to the vector field measurements of elastic corner vortices upstream of a 4:1:4 sharp contraction-expansion presented previously [5]. This reinforces our previous observations which indicate that once the lip vortex has reached the stagnant corner, the dynamics of the subsequent elastic vortex growth are identical to those observed in contraction ratios that do not demonstrate formation of a distinct lip vortex.

The dimensionless reattachment length and coordinates of the vortex center are shown in Figure 11. These measurements quantify the spatial characteristics observed in the pseudo streak images. At low Deborah numbers, the dimensionless reattachment length is again constant with the expected value for the Newtonian Moffatt vortex. As the Deborah number is increased, the reattachment length decreases drastically as the lip vortex begins to develop. At this point, the coordinates reported in Figure 11 shift from the disappearing Moffatt vortex to the center of the now-dominant and topologically-distinct lip vortex. As the lip vortex grows outward, the reattachment length remains quite small and the axial position of the lip vortex center remains relatively constant. Once the lip vortex has reached the stagnant corner, the radial location of the vortex center saturates at *?* - 1.5 and the large elastic corner vortex begins to grow upstream. Previous experimental measurements [16; 17] indicate that the lip vortices are unsteady in time and three dimensional in nature, but within the sensitivity of our velocity and pressure measurement techniques, the lip vortex resulting from the flow of a PS/PS solution through a 2:1:2 contraction-expansion is found to be steady in time. The difference may be a consequence of the difference in operating procedure; earler studies imposed a constant pressure difference ? P_{ud} across the contraction geometry and determined an average flow rate or velocity, whereas in the present experiments we use a fixed displacement rate and measure the ensuing pressure drop.

3.3. Laser Doppler Velocimetry Measurements

Axial velocity measurements taken along the centerline of the 4:1:4 axisymmetric abrupt contraction-expansion are shown in Figure 12. The dimensionless velocity measurements, $v_z/\langle v_z \rangle_2$, are plotted from locations far upstream of the contraction plane, $z/R_2 >$! 10, to positions inside the throat, z/R_2

= 0.25. In a Poiseuille flow, the velocity on the centerline is equal to twice the average velocity in the tube $v_z(r = 0) = 2\langle v_z \rangle$. Therefore, one would expect that for a constant viscosity fluid, the dimensionless centerline velocity well upstream of the contraction plane would be equal to $v_z/\langle v_z \rangle_2 = 2/ß^2 = 0.125$, while the dimensionless velocity within the throat would be equal to $v_z/\langle v_z \rangle_2 = 2$. This is confirmed far upstream, where the shear rate is quite low and where there are no extensional effects influencing the velocity profile. As the fluid approaches the contraction, the velocity increases to conserve mass as the radius of the tube abruptly contracts. At low Deborah numbers, this increase is observed to occur smoothly, beginning at an axial position of z/R_2 . ! 2.5. With the initial increase in Deborah number, the velocity increase shifts slightly downstream towards the contraction plane; however, as the flow rate is increased further, the velocity gradient along the centerline is reduced and the influence of the contraction is felt by the flow further and further upstream. This latter effect takes place in conjunction with the elastic vortex growth observed in §3.2. As the fluid enters the throat, there is a sharp elastic overshoot in the velocity at all Deborah numbers, including a small jump in the low Deborah number case, $De = 0.5$. The magnitude of this overshoot increases with Deborah number, but the location of the maximum does not change. Further downstream, the centerline velocity reduces to a value consistent with Poiseuille flow, for all but the highest Deborah numbers in which the velocity remains slightly high than $v_z/\langle v_z \rangle_2 = 2$ for the range of axial positions that can be measured with the present apparatus. Additional LDV measurements show that, the non-monotonic trend in the evolution of the centerline velocity profile is independent of contraction ratio and re-entrant corner curvature.

3.4. Flow Stability

While studying the flow of the PS solution into both the 4:1:4 and the 8:1:8 contraction-expansions,

a slow non-symmetric precession of the enlarged corner vortex was visually observed at large Deborah numbers. It should be reiterated here that within the sensitivity of our LDV and pressure measurements the 2:1:2 contraction-expansion was found to be stable at all Deborah numbers tested. This does not preclude the possibility of observing the instability at a higher Deborah number or possibly with more sensitive measurement techniques.

The onset of an elastic instability is first indicated by small amplitude oscillations in the global pressure drop and local velocity measurements which are observed to grow in magnitude with increasing Deborah number. In Figure 13(a), two samples of the temporal variation of the radial, $v_r(t)$, and axial, $v_z(t)$, velocity for the flow of the PS/PS Boger fluid into the 4:1:4 sharp contraction-expansion are shown at Deborah numbers of De = 3.5 and 7.0. These two measurements were taken at a position, (r/R_2, z/R_2) = (0.63, -1.26), just above the re-entrant corner. A fast Fourier transform (FFT) of the velocity data allows a quantitative determination of the frequency and amplitude of the velocity fluctuations. In Figure 13(b) we show the power spectral density (PSD) at De = 3.5. The Fourier spectrum indicates that the elastic flow instability has a strong fundamental oscillation frequency, f_1 = 0.15Hz, and the existence of a small peak at the first harmonic. As the Deborah number is further increased, the intensity of the velocity fluctuations grows in amplitude, the fundamental frequency of oscillation slowly increases and the higher harmonics of the fundamental frequency begin to appear. At a Deborah number of De = 7.0, the PSD plot in Figure 13(c) contains four detectable harmonics of the fundamental frequency.

The variation in the amplitude and frequency of oscillation determined from the Fourier spectrum, such as those shown in Figure 13(a) and (b) can be used to determine the critical Deborah number for the onset of this supercritical Hopf bifurcation, are shown in Figures 14 and 15 respectively. The critical

Deborah number for the onset of the periodic flow is accurately determined by fitting the these results to the asymptotic results for a supercritical Hopf bifurcation [29]

$$\left|\mathbf{v}(r,q,z,t)\right| \propto \left(De - De_{crit}\right)^{1/2}, \tag{8}$$

$$f = c_1 + c_2\left(De - De_{crit}\right), \tag{9}$$

where c_1 and c_2 are constants. These expressions are valid only in the linear limit, such that $(De - De_{crit}) << 1$. Theoretically, in this limit only the fundamental frequency will exist in the Fourier spectrum, however, a small first harmonic peak is present in the experiments at all but the very lowest unstable flow rate. To circumvent this difficulty, a cutoff for linearity is defined such that only data taken at Deborah numbers for which the amplitude of velocity fluctuations of the fundamental frequency are an order of magnitude greater than those of the first harmonic, $\left|\mathbf{v}(r,q,z,t)\right|_{f_0} > 10\left|\mathbf{v}(r,q,z,t)\right|_{2f_0}$, are used to determine De_{crit} from Equations 8 and 9. The results of these fits are superimposed on the data in Figures 14 and 15 and the critical Deborah numbers are tabulated in Table 4.

	Critical Deborah Number for the Onset of the Elastic Flow Instability
4:1:4 Sharp Contraction-Expansion	2.4 ± 0.1
4:1:4 Rounded Contraction-Expansion	3.1 ± 0.2
8:1:8 Contraction-Expansion	4.2 ± 0.2

Table 4: Critical conditions for the onset of the supercritical Hopf bifurcation.

The initial deviation from axisymmetric stable flow conditions is well describe by linear stability analysis. However, when $De >> De_{crit}$ nonlinear dynamics begin to dominate the flow kinematics. These nonlinear effects are first observed in the Fourier spectrum as higher harmonics of the fundamental frequency and the transition from a periodic to a period-doubling instability [16]. Another manifestation of these nonlinear dynamics observed in the present experiments is the development of a high speed 'jetting' instability near the lip of the contraction in the 4:1:4 contraction-expansion, which has not been reported previously. After the onset of the elastic flow instability, the upstream vortex breaks symmetry and begins to precess in the azimuthal direction. The extent of this symmetry breaking in the vortex height increases with Deborah number. In conjunction with the break in symmetry, a strong jet of high speed fluid appears, originating from the base of the upstream vortex and flowing directly into the throat just upstream of the contraction plane. By focusing the LDV probe at a position $(r/R_2, z/R_2) = (1.57, -0.16)$ within the vortex and just upstream of the contraction plane, it is possible to quantify this jetting flow instability. Measurements of the time-varying radial velocity are shown in Figure 16(a). The flow is initially steady with a velocity v_r . 3.5 mm/s ($v_r/\langle v_r \rangle_2$. 0.063) directed radially outward, indicating that the probe is focused within the recirculating region of the corner vortex. As the flow develops, the jetting flow appears as large amplitude periodic spikes in the velocity measurements. These spikes are larger in magnitude, v_r . ! 10 mm/s ($v_r/\langle v_r \rangle_2$. 0.18), than the stable recirculating flow velocity and directed inward toward the contraction entrance. The Fourier spectrum presented in Figure 16(b) contains several higher harmonics of the fundamental frequency including a first harmonic signal, the amplitude of which is nearly equivalent to that of the fundamental frequency. The fundamental frequency of the jetting instability is identical to the frequency of the upstream vortex precession. We therefore postulate that this instability is in fact a helical

jet of fluid running the entire axial length of the upstream vortex.

Two streak images and a DPIV vector field showing this instability can be found in Figure 17. The global structure of the unstable vortex is seen in Figures 17(a) and a box is sketched around the location of the jetting instability which appears at the base of the precessing asymmetric upstream vortex at the point of its greatest upstream extent. This box also indicates the field of view blown up in the streak image of Figure 17(b) and the vector field in Figure 17(c). Although these close-up images were taken at the same Deborah number as the full field of view, the images were not collected simultaneously and a slight difference in the temporal development of the jetting instability was unavoidable. The vectors in Figure 17(c) are scaled such that an arrow of length $l/R_2 = 0.5$ corresponds to a velocity of $v/\langle v_z \rangle_2 = 1$ and clearly demonstrate the strong localized nature of this instability. For a brief video clip of this instability we encourage the reader to either visit our website [30] or to contact the authors directly.

4. Discussion

In this work, we have presented a comprehensive set of experimental measurements of the complex flow of a dilute monodisperse polystyrene solution into axisymmetric contraction-expansions of various contraction ratios and re-entrant corner curvatures. The rheological properties of the test fluid have been well characterized in both shear and extension, making these experiments a demanding comparative tool for constitutive models and numerical simulations.

An enhanced pressure drop associated with the extensional flow of the viscoelastic fluid across an axisymmetric contraction-expansion but not directly connected with the onset of an elastic instability was observed for all geometries tested. Measurements of the flow kinematics for each geometry were also made with streak images, LDV and DPIV. The general evolution of the pressure drop measurements and the flow kinematics were found to be independent of the radius of curvature of the re-entrant corner, although the critical conditions for the transitions in pressure drop and vortex growth are a function of both the lip curvature and the contraction ratio. LDV and pressure drop measurements were used to characterize a supercritical Hopf bifurcation at large Deborah numbers which resulted in a global elastic instability, breaking the symmetry of the large enhanced upstream vortex and precessing in the azimuthal direction. This instability was observed for the 4:1:4 and 8:1:8 contraction-expansions irrespective of lip curvature. The 2:1:2 contraction-expansion was found to be stable up to the maximum Deborah numbers that could be tested.

4.1. Scaling of the Effects of Lip Curvature

The experiments with curved re-entrant corners support earlier observations in PIB/PB [13; 16] and PAA/CS elastic fluids [3; 13; 20] and suggest that numerical simulations should be able to remove the

singularity associated with the sharp re-entrant corner without affecting the ability of the constitutive model to predict the large enhanced viscoelastic pressure drop seen in experiments. The qualitative similarity seen in Figures 5, 6 and 7 between the evolution in the vortex dimensions (*?*, *?* and *?*) and the extra pressure drop (P) with increasing Deborah number in the 4:1:4 contraction-expansions with sharp and rounded re-entrant corners suggest that it should be possible to collapse the data into a single generic response for a given contraction ratio. The principal effect of smoothing the re-entrant corner is to increase the radius of curvature and decrease the rate of deformation along the streamlines entering the contraction by removing the re-entrant corner singularity. For a low Reynolds number flow, an appropriate estimate of the residence time for a fluid element in the vicinity of the curved throat region is given by $T \sim (R_2+R_c)/\langle v_z \rangle_2$. The Deborah number then becomes $De = ?\langle v_z \rangle_2/(R_2+R_c)$. This simple scaling of the abscissa does a remarkable job of collapsing the vortex growth data for the 4:1:4 sharp and rounded re-entrant corners onto a single curve, as shown in Figures 18(a), even matching the transition to time-dependent flow.

Changing the local curvature of the lip entrance also affects the value of the entrance pressure drop for the creeping flow of a Newtonian fluid that is used to scale the ordinate axis in Figure 18(b). As defined in Equation 2, the dimensionless pressure drop tends to be underpredicted ($P < 1$) for geometries with curved re-entrant lips. Comparison of the dimensionless pressure drop data after appropriately shifting the Deborah number in the manner described above supports the expectation that the extra pressure drop at high Deborah numbers following upstream vortex growth is independent of the specific details of the local lip curvature. The principal effect of the lip is experienced at low Deborah number when the converging flow near the contraction plane is of the Sampson type. The dimensionless pressure drop (which we always

scale with the Sampson flow solution for entrance in a sharp orifice ? $P_S = 3?_0 Q/R_2^3$) can thus be adjusted through the addition of a Couette-like, creeping flow correction, $C_s(ß, R_c) = P_{sharp}(De = 0) ! P_{curved}(De = 0)$, to take into account the pressure drop corresponding to the Newtonian flow through the curved entrance region. In Figure 18(b), the results of this scaling of the dimensionless pressure drop $P_{shifted} = P_{curved} + C_s(ß, R_c)$ is shown for two cases: the 4:1:4 sharp and rounded contraction-expansions where the Couette-like correction was found from experiments to be $C_s(R_c/R_2 = 0.5, ß = 4) = 0.35$ and the sharp and rounded 8:1:8 contraction-expansions where $C_s(R_c/R_2 = 0.18, ß = 8) = 4.6$. The latter data are presented to demonstrate the robustness of this scaling over several contraction ratios and radii of curvature. It is dangerous to generalize based on experimental data with only two values of radius of curvature ($R_c = 0.18R_2$ and $0.5R_2$), but this rescaling of the Deborah number also collapses quite well the trends of vortex reattachment length reported in the literature for PIB/PB Boger fluids [16]. It would be very interesting to see if this simple incorporation of curvature effects on vortex size and pressure drop is supported by numerical calculations in which the radius of curvature of the re-entrant corner is systematically varied over a broad range.

4.2. The Role of Transient Extensional Viscosity

With variations in the contraction ratio, the flow field upstream of the contraction-expansion was found to evolve along two distinct vortex growth pathways. For a contraction ratio of $b = 2$ a steady elastic lip vortex was observed, while for contraction ratios of $4 # b # 8$ a corner vortex was seen. The presence or the absence of a lip vortex has been noted in many different studies and depends not only on the contraction ratio through which the fluid is forced, but also on the formulation of the fluid used. These observations are summarized in Table 2 which, when completed with the vortex growth data for the PS/PS

Boger fluid from this study, shows a marked similarity between the behavior of the PS/PS and PAA/CS test fluids. It has been conjectured that the differences in flow transitions for fluids with ostensibly identical shear properties question must arise from differences in extensional rheology [5; 16; 31]. This hypothesis suggests that the differences observed in contraction flows and other complex flows arise from changes in the molecular characteristics of the equilibrium conformations of the polymer chains resulting from solvent quality or stiffness of the polymer backbone [13; 18; 32]. It follows that these initial equilibrium conformational differences will also have a large effect on the evolution of non-equilibrium properties such as the transient extensional stress growth in the fluid. With the advent of the filament stretching rheometer and the advances in simulation techniques for bead-rod and bead-spring models, it is now possible to probe such hypotheses both experimentally and numerically [33].

A fluid filament experiencing a constant uniaxial extension rate in a filament stretching rheometer should, at least qualitatively, describe the uniaxial elongation of the fluid element flowing along the centerline into the contraction-expansion even if the extension rate in this case is not constant. If one assumes a fully developed Poiseuille flow in the throat of the axisymmetric contraction-expansion, then one can calculate the total Hencky strain experienced by a fluid element moving along the centerline from far upstream into the middle of the throat as

$$e = \int_0^{t_1} \dot{e}\, \mathrm{d}t = \int_{v_z(z=-\infty)}^{v_z(z=0.5L_c)} \frac{\mathrm{d}v_z}{v_z} = 2 \ln b. \qquad \textbf{(10)}$$

Dotted lines representing the total accumulated strain of a fluid element traveling along the centerline into each of the geometries tested are superimposed over the extensional rheology data in Figure 19. These measurements seem to reinforce our previous conjecture. The PS/PS solution flowing into the 2:1:2

contraction-expansion demonstrates no significant strain-hardening while the extensional viscosity of the PS/PS solution flowing into the 4:1:4 and especially the 8:1:8 contraction-expansions is greatly enhanced. Thus, in the case of a PS/PS test fluid, a simple doubling of the extensional viscosity along the centerline is enough to eliminate the lip vortex. If this result could be generalized to other polymeric fluids, real physical insight might be achieved. Unfortunately, in similar extensional rheology tests of the same PIB/PB Boger fluid used by McKinley et al. [16] which are also shown in Figure 19, the lip vortex is present at all contraction ratios, $ß < 8$, corresponding to Trouton ratios up to $Tr \approx 150$; well past the Trouton ratio at which the flow of the PS/PS Boger fluid begins to demonstrate elastic corner vortex growth.

Although these two fluids demonstrate similar behaviors in extension, it is still important to point out their differences. The Trouton ratio of the monodisperse, dilute PS/PS solution grows more quickly and can be up to 50% larger than the Trouton ratio of polydisperse, semidilute PIB/PB at moderate Hencky strains. Li and Larson [33] used a bead-spring simulation to show that for a dilute high molecular weight polymer dissolved in a good solvent, both the stress and the birefringence rise much more rapidly with strain than for the same polymer dissolved in a theta solvent. Differences in solvent quality between these two Boger fluid formulations, the PS being dissolved in a slightly better solvent than the PIB, may still hold the key to differences in the kinematics and the dynamics of the flow. The effect of solvent quality has been systematically investigated in several model complex flows, for example viscoelastic flow past falling spheres. In a series of experiments performed by Solomon and Muller [32] using high molecular weight PS fluids, the increase in the drag coefficient above that expected for a Newtonian fluid was found to increase with increasing solvent quality. Unfortunately, this argument is not entirely consistent throughout the literature. Chmielewski et al. [18] compared the drag past a falling sphere for two different Boger fluids. They found that the drag increased over the Newtonian value for the PIB solution in a close to theta

solvent (polybutene), but the drag decreased below Newtonian for a PAA solution in a good solvent (corn syrup/water). These results are not consistent with our argument which would hold that because the PAA is dissolved in a better solvent than the PIB and it should demonstrate a more rapidly strain hardening extensional viscosity and a larger drag coefficient. The difference in this case may be the result of the shear thinning in the solution viscosity of the PAA/CS/H_2O fluid which is of the same order of magnitude (25%) as the reduction in drag.

In our experiments, the enhanced pressure drop measurements across the contraction-expansions were found to be qualitatively independent of both the contraction ratio and the radii of curvature of the re-entrant corner. However, even with rounded re-entrant corners, these large additional pressure drops have not been predicted by any existing numerical simulations using simple dumbbell models [7-9]. The evidence suggests that these discrepancies arise because of the inability of current bead-spring constitutive models to properly describe the extensional rheology of the polymer solutions. Most notable is the failure of these constitutive models to qualitatively predict the stress-conformation hysteresis first observed by Doyle et al. in measurements of uniaxial transient elongation [10; 11]. To capture such effects it may be necessary to resolve the non-equilibrium internal dynamical structure of the polymer chains recently observed by Perkins et al. [34] by performing simulations with bead-rod chain models that can capture such 'configurational hysteresis'. However, an excellent description of the extensional viscosity alone might not be adequate to accurately model the flow into an axisymmetric contraction-expansion. Observations of the polystyrene Boger fluid in transient uniaxial extensional demonstrate no sign of strain hardening or of the dissipative stress suggested by stress-conformation hysteresis at the small strains achieved by a fluid element traveling along the centerline of the 2:1:2 axisymmetric contraction-expansion (e = 1.386) and yet the pressure drop measurements still show a dramatic enhancement. Presumably, this results from the much larger

deformations experienced by fluid elements passing near the re-entrant corner singularity but this cannot be confirmed until simulation are performed using a suitable constitutive model.

4.3. The Normal Stress Ratio

A combined knowledge of the shear and extensional properties of these polymeric fluids should ideally provide a means of predicting the vortex growth dynamics *a priori*. As the contraction ratio is increased at a fixed Deborah number, the shear rate at the tube walls upstream of the contraction decreases as $\dot{g}_1 \propto \frac{1}{b^3}$, while at the same time, the accumulated strain along the centerline increases as $e \% \ln ß$. Thus, there are two competing effects which contribute to the fluid's choice of vortex growth evolution; namely, extensional stresses and shear induced normal stresses. It is clear from these simple estimates of the strain and deformation that a lip vortex is present for elastic test fluids for contraction ratios which generate very little extension of the polymer chain along the centerline; they may therefore be considered to be elastically shear-dominated. For a given contraction ratio, the extensional stresses increase dramatically as the Deborah number is increased; whereas, for most Boger fluids, the first normal stress difference tends to saturate due to shear thinning arising from finite extensibility effects. A large elastic vortex then supplants the lip vortex. Similarly, as the contraction ratio is increased, the extensional stresses developed within the contraction flow dominate the normal stress difference arising from shear and, once again, a corner vortex replaces the lip vortex.

We have argued that the flow kinematics associated with the transition from lip to corner vortex appear to be driven by a change in the dynamics from a shear dominated to an extension dominated flow. A possible means of quantifying this transition is to compare the normal stresses generated by the shear flow along the walls to the extensional stresses resulting from the elongational flow along the centerline. We thus consider a dimensionless normal stress ratio defined as

$$\aleph = \frac{N_1 / h_0 \dot{\gamma}}{\left(t_{zz} - t_{rr}\right) / h_0 \dot{\varepsilon}} = \frac{S_R(\dot{\gamma})}{T_R(\varepsilon)}, \qquad \textbf{(11)}$$

where T_R(e) is the Trouton ratio evaluated at the total Hencky strain accumulated along the centerline of the contraction-expansion and $S_R(\dot{\gamma})$ is the shear-rate-dependent stress ratio. Although, we differentiate explicitly between the extension rate $\dot{\varepsilon}$ and the shear rate $\dot{\gamma}$, in a nonhomogeneous flow, such as the one considered here, it is sufficient to approximate both as $\dot{\gamma} \cdot \dot{\varepsilon} \cdot \langle v_z \rangle_2/(R_2 + R_c)$. Arigo and McKinley [37] used this dimensionless group to help rationalize the differences in the wake developing downstream of spheres sedimenting in dilute and concentrated viscoelastic fluids, however, to our knowledge it has not been used to compare differences between different ideal elastic Boger fluids. In Figure 20, the normal stress ratio ($\aleph$) is plotted as a function of contraction ratio for the PS/PS, PIB/PB and PAA/CS Boger fluids used in contraction flow publications [5; 13; 16; 20]. Of course, this normal stress ratio is also a function of deformation rate and should be represented as a two-dimensional surface, $\aleph(b, De)$. Here we have chosen to evaluate the normal stress number at the deformation rate ($\langle v_z \rangle_2/R_2$) corresponding to the onset of the first significant elastic vortex growth. The shear and extensional rheological data used to calculate the normal stress number for the PIB/PB and PS/PS Boger fluids can be found in Figures 2, 3 and 19 and in McKinley et al. [16], while analogous shear and extensional rheology data for PAA/CS Boger fluids can be found in Stokes [38]. The PAA/CS Boger fluids characterized by Stokes [38] are similar, but not identical, to the test fluids used by Nguyen and Boger [20], so two representative solutions denoted Fluid C (η_0 = 1.5Pa·s) and Fluid E (η_0 = 23Pa·s) by the author have been chosen for comparison. Note that the extensional rheology of PAA/CS solutions is extremely difficult to measure in a filament stretching rheometer because of the tendency of the corn syrup solvent to crystallize at the surface of the fluid filament. At low Hencky strains, the resulting 'skin' on the PAA/CS filament results in an

overprediction of the Trouton ratio and a large uncertainty in the normal stress ratio for the 2:1 contraction. At moderate to large Hencky strains ($e \geq 3$), however, the skin does not affect the extensional data.

It can be seen from Figure 20, that there is a marked difference between the normal stress ratio calculated for the PS/PS and the PAA/CS solutions and for the PIB/PB solution. The normal stress ratio decreases monotonically with contraction ratio. For an ideal elastic liquid, which can be modeled at the most elementary level by the Oldroyd-B model, χ can be expressed analytically for $De > 0.5$ by the following expression

$$\chi \simeq \frac{2h_p l_1 \dot{\gamma}^2}{3h_s\dot{\varepsilon} + \frac{h_p\dot{\varepsilon}}{2 l_1\dot{\gamma} - 1}\exp\left[2\varepsilon\left(1-(2 l_1\dot{\varepsilon})^{-1}\right)\right]} = \frac{2(h_p/h_s)De}{3+\frac{(h_p/h_s)}{2De-1}\exp\left[2\varepsilon\left(1-(2De)^{-1}\right)\right]} \qquad \textbf{(12)}$$

where $\dot{\gamma} \cdot \dot{\varepsilon} \cdot \langle v_z\rangle_2/(R_2 + R_c)$ and $\varepsilon = 2\ln\beta$. The magnitude of this ratio thus depends on the ratio η_p/η_s (which depends on solvent quality and polymer concentration), the Deborah number and the contraction ratio.

Over the entire range of contraction ratios examined, the normal stress ratio of the PS/PS and PAA/CS solutions are significantly smaller than the normal stress ratio of the PIB/PB solution. A line can be drawn through the data at a normal stress ratio of $\chi \cdot 0.055 \pm 0.005$ which divides the data into regimes of elastic corner vortex growth ($\chi \cdot 0.055$) and lip vortex growth ($\chi / 0.055$). As the Deborah number, and subsequently the tensile normal stress difference in extension, increase, we expect the normal stress ratio to decrease monotonically and the lip vortex regime to eventually give way to elastic corner vortex growth. This is the first quantitative evidence to suggest that the kinematics of the flow can be systematically rationalized on the basis of rheological information. It would be interesting to compare these observations with Brownian dynamics computations of the ratio of elastic stress differences in shear to first normal stress

differences in extension as the solvent quality or excluded volume is systematically modified.

The pressure drop measurements, LDV and DPIV measurements, and the streak images coupled with the use of a monodisperse dilute polymer solution, well characterized in shear and extension, make this set of experiments, in conjunction with our previous work [5], a useful tool for forming comparisons with theoretical and numerical work. The principal remaining difference between different experimental observations of the lip vortex is now the time-dependent characteristic observed in different elastic fluids. Possible explanations here may include the method of observation used (e.g. time-averaged streak photography or time-resolved LDV and DPIV measurements) and, perhaps more importantly, the driving mechanism used. In the present work, we use a constant volumetric displacement rate, whereas the majority of previous studies have imposed a constant global pressure drop across the test geometry. This important difference in experimental control parameters leads to different dynamics in many other bifurcating systems (e.g. spurt and stick slip in melt extrusion) and may prove to be a useful avenue for future research studies.

Acknowledgments

The authors wish to acknowledge financial support from NASA under grant NCC3-610, Dr. Shelley Anna of Harvard University for kindly supplying us with the transient uniaxial elongation measurements and Professor D.P. Hart of MIT for the use of his DPIV algorithm.

References

[1] O. Hassager. Working group on numerical techniques, Fifth International Workshop on Numerical Methods in Non-Newtonian flows, Lake Arrowhead, USA, J. Non-Newtonian Fluid Mech., **29** (1988) 2-5.

[2] B. Caswell. Report on the IXth International Workshop on Numerical Methods in Non-Newtonian

Flows, J. Non-Newtonian Fluid Mech., **62** (1996) 99-110.
[3] D.V. Boger. Viscoelastic flows through contractions, Annual Review of Fluid Mechanics, **19** (1987) 157-182.
[4] S.A. White, A.D. Gotsis and D.G. Baird. Review of the entry flow problem: experimental and numerical, J. Non-Newtonian Fluid Mech., **24** (1987) 121-160.
[5] J.P. Rothstein and G.H. McKinley. Extensional flow of a polystyrene Boger fluid through a 4:1:4 axisymmetric contraction/expansion, J. Non-Newtonian Fluid Mech., **86** (1999) 61-88.
[6] U. Cartalos and J.M. Piau. Creeping flow regimes of low concentration polymer solutions in thick solvents through an orifice die, J. Non-Newtonian Fluid Mech., **45** (1992) 231-285.
[7] P. Szabo, J.M. Rallison and E.J. Hinch. Start-up of flow of a FENE-fluid through a 4:1:4 constriction in a tube, J. Non-Newtonian Fluid Mech., **72** (1997) 73-86.
[8] P.J. Coates, R.C. Armstrong and R.A. Brown. Calculation of steady-state viscoelastic flow through axisymmetric contractions with the EEME formulation, J. Non-Newtonian Fluid Mech., **42** (1992) 141-188.
[9] R.A. Keiller. Entry-flow calculations for the Oldroyd-B and FENE equations, J. Non-Newtonian Fluid Mech., **46** (1993) 143-178.
[10] P.S. Doyle, E.S.G. Shaqfeh, G.H. McKinley and S.H. Spiegelberg. Relaxation of dilute polymer solutions following extensional flow, J. Non-Newtonian Fluid Mech., **76** (1998) 79-110.
[11] T. Sridhar, D.A. Nguyen and G.G. Fuller. Birefringence and stress growth in uniaxial extension of polymer solutions, J. Non-Newtonian Fluid Mech., **90** (2000) 299-315.
[12] L. Li, R.G. Larson and T. Sridhar. Brownian dynamics simulations of dilute polystyrene solutions, J. Rheol., **44** (2000) 291-322.
[13] D.V. Boger and R.J. Binnington. Experimental removal of the re-entrant corner singularity in tubular entry flows, J. Rheol., **38** (1994) 333-349.
[14] B. Purnode and M.J. Crochet. Flows of plymer solutions through contractions. Part 1: Flows of polyacrylamide solutions through planar contractions., J. Non-Newtonian Fluid Mech., **65** (1996) 269-289.
[15] J.V. Lawler, S. J. Muller, R. A. Brown and R.C. Armstrong. Laser Doppler Velocimetry Measurements of Velocity Fields and Transitions in Viscoelastic Fluids, J. Non-Newtonian Fluid Mech., **20** (1986) 51-92.
[16] G.H. McKinley, W.P. Raiford, R.A. Brown and R.C. Armstrong. Nonlinear dynamics of viscoelastic flow in axisymmetric abrupt contractions, J. Fluid Mech., **223** (1991) 411-456.
[17] D.V. Boger and R.J. Binnington. Circular entry flows in fluid M1, J. Non-Newtonian Fluid Mech., **35** (1990) 339-360.
[18] C. Chmielewski, K.L. Nichols and K. Jayaraman. A comparison of the drag coefficients of spheres translating in corn-syrup-based and plybutene-based Boger fluids, J. Non-Newtonian Fluid Mech., **35** (1990) 37-49.
[19] S.L. Anna, G.H. McKinley, D.A. Nguyen, T. Sridhar, S.J. Muller, J. Huang and D.F. James. An inter-laboratory comparison of measurements from filament stretching rheometers using common test fluids, J. Rheol., (2000) (In Preparation).
[20] H. Nguyen and D.V. Boger. The Kinematics and Stability of Die Entry Flows, J. Non-Newtonian Fluid Mech., **5** (1979) 353-368.
[21] M.T. Arigo, D. Rajagopalan, N. Shapley and G.H. McKinley. The sedimentation of sphere

through an elastic fluid .1. Steady motion, J. Non-Newtonian Fluid Mech., **60** (1995) 225-257.
[22] D.V. Boger. A highly elastic constant-viscosity fluid, J. Non-Newtonian Fluid Mech., **3** (1977/78) 87-91.
[23] B.H. Zimm. Dynamics of polymer molecules in dilute solution: viscoelasticity, flow birefringence and dielectric loss, J. Chem. Phys., **24** (1956) 269-278.
[24] R.B. Bird, R.C. Armstrong and O. Hassager. Dynamics of Polymeric Liquids: Volume 1 Fluid Mechanics, John Wiley & Sons, New York, 1987.
[25] H.C. Ottinger. Generalized Zimm model for dilute polymer-solutions under theta-conditions, J. Chem. Phys., **86** (1987) 3731-3749.
[26] R.B. Bird and J.R. DeAguiar. An encapsulated dumbell model for concentrated polymer solutions and melts I. Theoretical development and constitutive equation, J. Non-Newtonian Fluid Mech., **13** (1983) 149-160.
[27] S.L. Anna, C.B. Rogers and G.H. McKinley. On controlling the kinematics of a filament stretching rheometer using a real-time active control mechanism, J. Non-Newtonian Fluid Mech., **87** (1999) 307-335.
[28] J. Happel and H. Brenner. Low Reynolds Number Hydrodynamics, Prentice-Hall Inc., Englewood Cliffs, NJ, 1965.
[29] G. Iooss and D.D. Joseph. Elementary Stability and Bifurcation Theory, Springer, New York, 1980.
[30] http://web.mit.edu/nnf/jetting_instability.avi
[31] D.V. Boger, D.U. Hur and R.J. Binnington. Further observations of elastic effects in tubular entry flows, J. Non-Newtonian Fluid Mech., **20** (1986) 31-49.
[32] M.J. Solomon and S.J. Muller. Flow past a sphere in polystyrene-based Boger fluids: the effect on the drag coefficient of finite extensibility, solvent quality and polymer molecular weight., J. Non-Newtonian Fluid Mech., **62** (1996) 81-94.
[33] L. Li and R. Larson. Excluded volume effects on the birefringence and stress of dilute polymer solutions in extensional flow, Rheol. Acta, **In Press** (2000)
[34] T.T. Perkins, D.E. Smith and S. Chu. Single Polymer Dynamics in an Elongational Flow, Science, **276** (1997) 2016-2021.
[35] S.L. Anna and G.H. McKinley. The evolution of tensile stresses and birefringence in uniaxial elongational flows of dilute polymer solutions subjected to a known preshear history, Proceedings of the XIIIth International Congress on Rheology, (2000)
[36] R.G. Larson. The role of molecular folds and "pre-conditioning" in the unraveling of polymer molecules during extensional flow, J. Rheol., **in Press** (2000)
[37] M.T. Arigo and G.H. McKinley. An experimental investigation of negative wakes behind spheres settling in a shear-thinning viscoelastic fluid, Rheol. Acta, **37** (1998) 307-327.
[38] J.R. Stokes, Swirling flow of viscoelastic fluids, Ph.D. Thesis, Melbourne, 1998.

A. List of Figure Captions

Figure 1: Schematic diagram of contraction geometry including definitions of important length scales.

Figure 2: Rheological material functions of the 0.025wt% monodisperse polystyrene in oligomeric polystyrene solution. The data include: €, steady shear viscosity, $\eta(\dot{\gamma})$ [Pa•s]; ~, dynamic viscosity, $\eta'(\omega)$ [Pa•s]; ", dynamic rigidity, $2\eta''(\omega)/\omega$ [Pa•s^2]; !, first normal stress coefficient, $\Psi_1(\dot{\gamma})$ [Pa•s^2]; and the corresponding fits of the FENE-P, – · –, Bird-DeAguiar, —, and Zimm model, – –, respectively.

Figure 3: Measurements of the dimensionless transient uniaxial extension, $\bar{h}^+ / h_0$, as a function of Hencky strain, $\varepsilon = \dot{\varepsilon} t$. The data include: •, experimental measurements of the 0.025wt% PS/PS solution taken at a strain rate of $\dot{\varepsilon} = 9.1 s^{-1}$; and – –, FENE-P model fit. The maximum strain achieved along the centerline of the three contraction ratios tested is also shown.

Figure 4: Dimensionless pressure drop measurements, $P(De, \beta, R_c) = \Delta P_{ud}(De, \beta, R_c) / \Delta P_{ud}(Q, De = 0, R_c = 0, b = 0)$, of the 0.025wt% PS/PS solution across several axisymmetric contraction-expansions as a function of Deborah number, $De = \lambda_0 \dot{\gamma}$. The figure includes: ", $\beta = 8$; ~, $\beta = 4$; and ª, $\beta = 2$. The hollow symbols represent stable flow conditions while the filled symbols represent unstable flow conditions.

Figure 5: Dimensionless pressure drop measurements, $P(De, \beta, R_c)$, of the 0.025wt% PS/PS solution across two 4:1:4 axisymmetric contraction-expansions with different entrance lip curvature as a function of Deborah number, $De = \lambda_0 \dot{\gamma}$. The figure includes: ~, $\beta = 4$ and $R_c = 0$; and ", $\beta = 4$ and $R_c = 0.5\ R_2$. The hollow symbols represent stable flow conditions while the filled symbols represent unstable flow conditions.

Figure 6: Streak images comparing the flow upstream of a 4:1:4 axisymmetric contraction-expansion with (a)-(c) a sharp entrance lip, $R_c = 0$, and (d)-(f) a rounded entrance lip, $R_c = 0.5\ R_2$, taken at identical Deborah numbers of (a),(d) $De = 1.6$, (b),(e) $De = 2.6$, and (c),(f) $De = 3.6$.

Figure 7: Characteristics of the upstream vortex growth dynamics as a function of Deborah number for the 4:1:4 axisymmetric contraction-expansion with rounded entrance lip, $R_c = 0.5\ R_2$,: !, vortex reattachment length, $\chi = L_v / R_2$; ª, radial location of the vortex center, $\chi = R_v / R_2$; ~, the upstream location of the vortex center, $\chi = Z_v / R_2$; and , , vortex reattachment length for the 4:1:4 contraction-expansion with sharp entrance lip, $R_c = 0$.

Figure 8: Characteristics of the upstream vortex growth dynamics as a function of Deborah number for the 8:1:8 axisymmetric contraction-expansion: !, vortex reattachment length, $\chi = L_v / R_2$; ª, radial location of the vortex center, $\chi = R_v / R_2$; and ~, the upstream location of the vortex center, $\chi = Z_v / R_2$.

Figure 9: Streak images of flow upstream of a 2:1:2 axisymmetric contraction-expansion for Deborah numbers of (a) $De = 0.6$, (b) $De = 0.9$, (c) $De = 1.1$ and (d) $De = 1.5$ showing the development and growth of the lip vortex.

Figure 10: Particle Image Velocimetry (PIV) measurements of the vector fields for the recirculating flow upstream of a 2:1:2 axisymmetric contraction-expansion at Deborah numbers of (a) De = 0.9 and (b) De = 1.5.

Figure 11: Characteristics of the upstream vortex growth dynamics as a function of Deborah number for the 2:1:2 axisymmetric contraction-expansion: !, vortex reattachment length, ? = L_v / R_2; a, radial location of the vortex center, ? = R_v / R_2; and ~, the upstream location of the vortex center, ? = Z_v / R_2.

Figure 12: Laser Doppler Velocimetry (LDV) measurements showing the dimensionless axial velocity along the centerline, $v_z/\langle v_z \rangle_2$, as a function of dimensionless axial position, z/R_2, for the flow through a 4:1:4 axisymmetric contraction-expansion. The figure includes: ~, Deborah number of De = 0.5; ", De = 1.0; a, De = 1.5; «, De = 2.0; ', De = 3.0; ¬, De = 4.0; and -, De = 5.0.

Figure 13: The onset of a supercritical elastic instability seen in (a) Laser Doppler Velocimetry (LDV) measurements of the flow upstream of a 4:1:4 axisymmetric contraction-expansion and power spectral density plots of (b) radial velocity measurements, v_r, at a Deborah number of De = 3.5 and (c) axial velocity measurements, v_z, at a Deborah number of De = 7.0.

Figure 14: Amplitude of velocity fluctuations in the unstable upstream flow into a 4:1:4 axisymmetric contraction-expansion as a function of Deborah number. The data include: €, experimental measurements, and —, the theoretical prediction for a supercritical Hopft bifurcation, $|\mathbf{v}| \sim (De - De_{crit})^{1/2}$.

Figure 15: Fundamental frequency of velocity and pressure drop fluctuations in the unstable upstream flow into the axisymmetric contraction-expansions as a function of Deborah number. The data include: €, v_z for the 4:1:4 sharp contraction-expansion; ~, v_r for the 4:1:4 sharp contraction-expansion; >, v_z for the 8:1:8 contraction-expansion; a, $v_?$ for the 8:1:8 contraction-expansion; •, ? p for the 4:1:4 rounded contraction-expansion; and —, the theoretical prediction for a supercritical Hopf bifurcation, $f \sim (De - De_{crit})$.

Figure 16: Nonlinear dynamics of jetting flow observed in (a) LDV measurements of the radial velocity at a position r/R_2 = 1.57 and z/R_2 = ! 0.16 upstream of the 4:1:4 axisymmetric contraction-expansion and the corresponding (b) power spectral density plot at a Deborah number of De = 4.5.

Figure 17: Streak images of the jetting instability upstream of a 4:1:4 axisymmetric contraction-expansion for Deborah numbers of De = 3.5 showing the (a) full view of the unstable upstream vortex and (b) a closeup of the jetting instability along with (c) PIV velocity vector field generated from the closeup images.

Figure 18: Master curves of (a) reattachment length and (b) dimensionless pressure drop measurements, P(De, ß, R_c), for the flow of the 0.025wt% PS/PS solution across two 4:1:4 axisymmetric contraction-expansions with different entrance lip curvature as a function of Deborah number shifted to account for re-entrant corner curvature (see text for details). The figures include: ~, ß = 4 and R_c = 0; ", ß = 4 and R_c = 0.5 R_2; a, ß = 8 and R_c = 0; and ', ß = 8 and R_c = 0.5 R_2.

Figure 19: Uniaxial extensional measurements of Transient Trouton ratio, $\bar{h}^+ / h_0$, as a function of Hencky

strain, $e = \dot{e}t$, for the 0.31wt% PIB/PB solution, ~, and the 0.025wt% PS/PS solution, •, taken at a Deborah number of $\lambda_Z \dot{e} = 27$, where λ_Z is the Zimm relaxation time. The maximum strain achieved along the centerline of the 2:1:2, 4:1:4 and 8:1:8 contractions-expansions are indicated by the dashed lines.

Figure 20: The normal stress ratio, $\chi = S_R/T_R$, as a function of contraction ratio evaluated at the deformation rate corresponding to the onset conditions for upstream vortex growth. The data includes: €, the 0.025wt% PS/PS solution ($\langle v_z \rangle_2/R_2 = 5.1s^{-1}$); C, the 0.31wt% PIB/PB solution ($\langle v_z \rangle_2/R_2 = 9.2s^{-1}$) from [16]; and two PAA/CS solutions >, Fluid C ($\langle v_z \rangle_2/R_2 = 0.14s^{-1}$) and ?, Fluid E ($\langle v_z \rangle_2/R_2 = 2.5s^{-1}$) from [38].

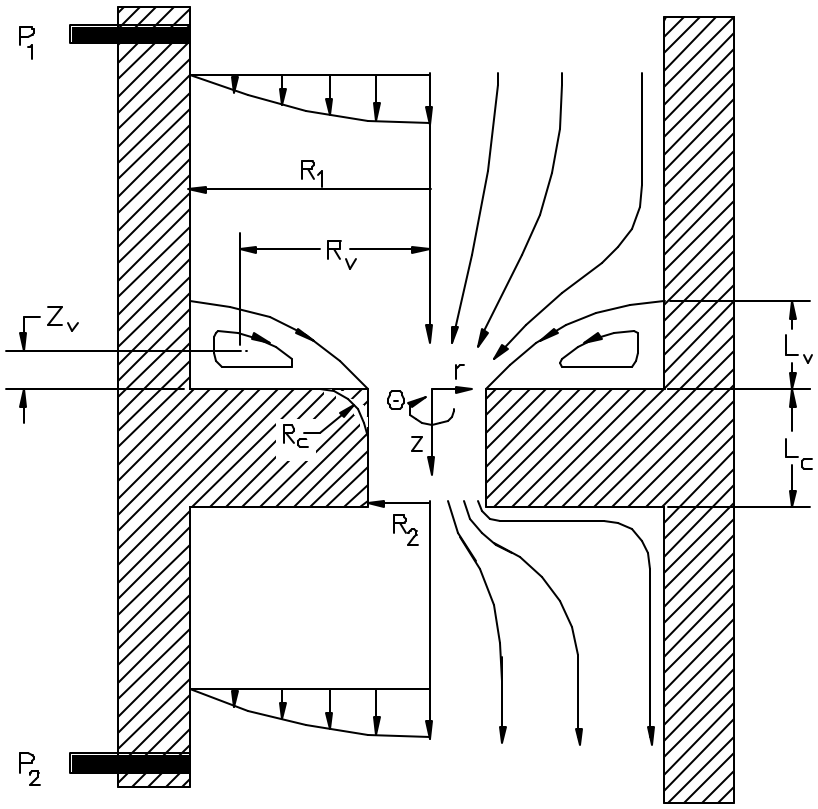

Figure 1

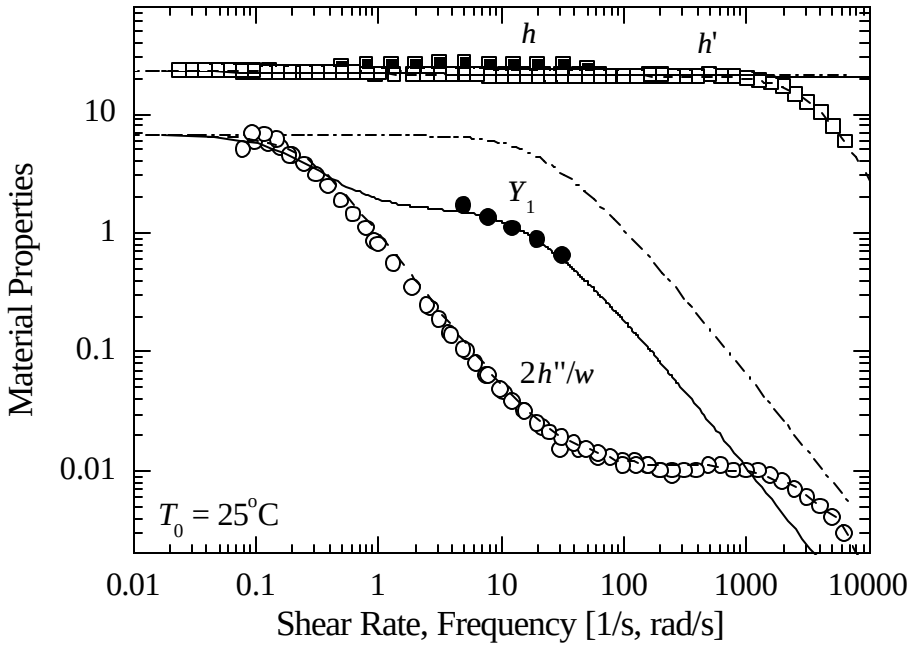
h
h'
10
1
0.1
0.01
Material Properties
Y1
2h''/w
T0 = 25°C
0.01
0.1
1
10
100
1000
10000
Shear Rate, Frequency [1/s, rad/s]

Figure 2

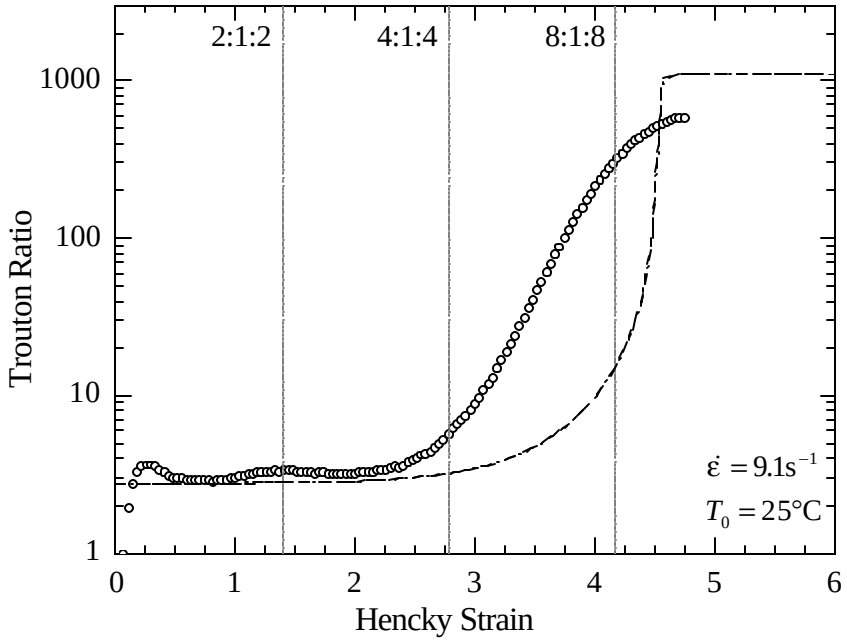
2:1:2
4:1:4
8:1:8
1000
100
10
1
Trouton Ratio
0
1
2
3
4
5
6
Hencky Strain
$\dot{\varepsilon} = 9.1 s^{-1}$
$T_0 = 25°C$

Figure 3

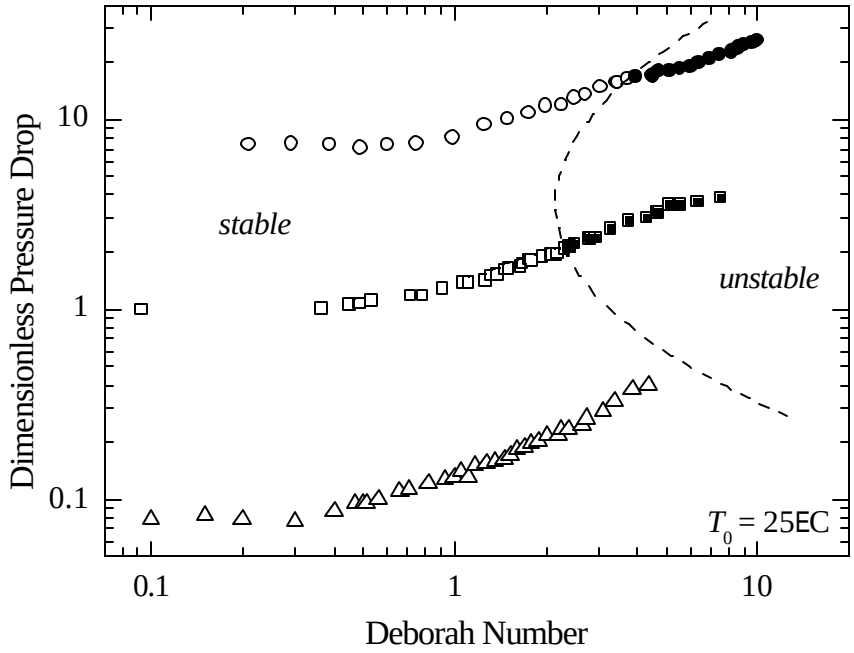
Dimensionless Pressure Drop
10
1
0.1
stable
unstable
T_0 = 25EC
0.1
1
10
Deborah Number

Figure 4

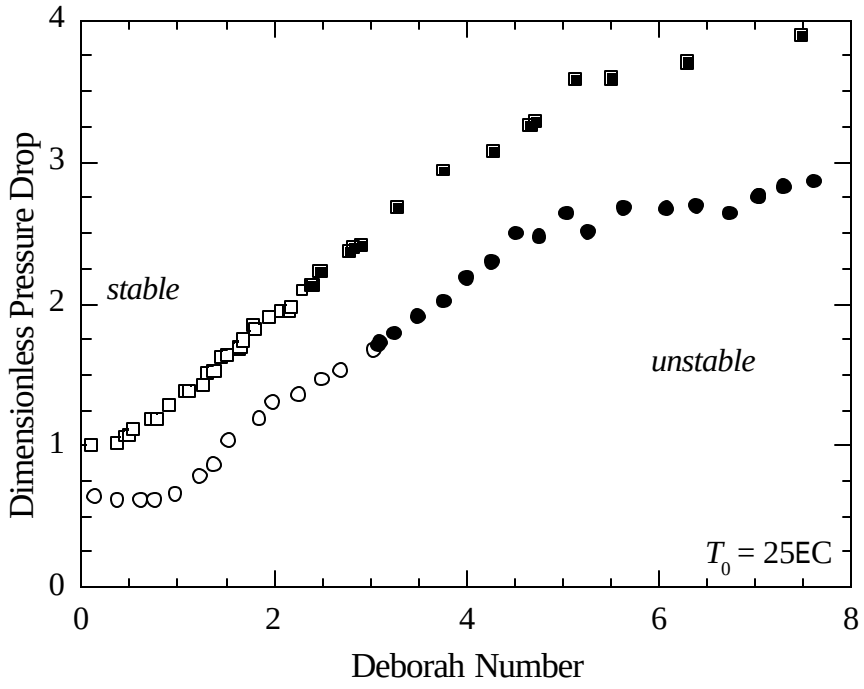
Dimensionless Pressure Drop
Deborah Number
stable
unstable
T_0 = 25EC
0
1
2
3
4
0
2
4
6
8

Figure 5

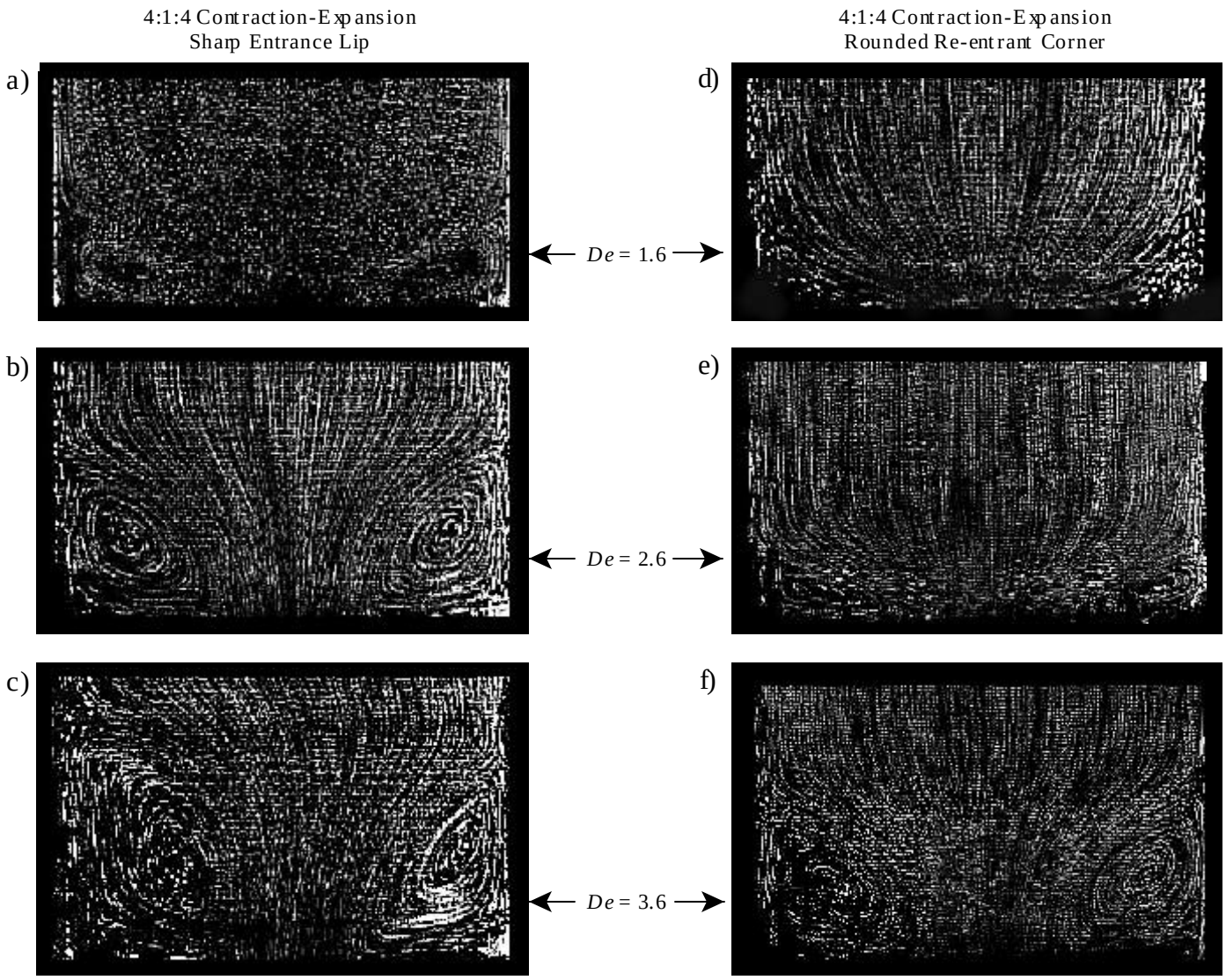
4:1:4 Contraction-Expansion
Sharp Entrance Lip
4:1:4 Contraction-Expansion
Rounded Re-entrant Corner
a)
d)
De = 1.6
b)
e)
De = 2.6
c)
f)
De = 3.6

Figure 6

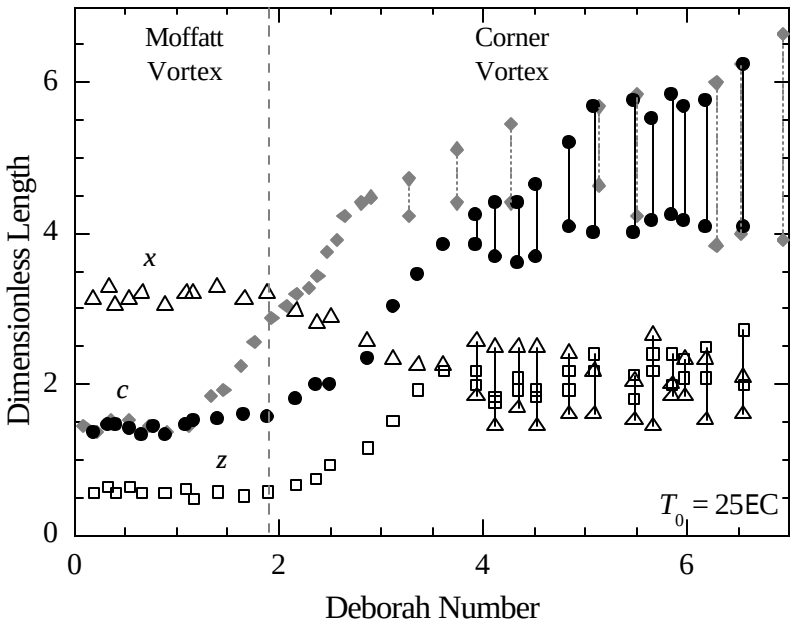
Moffatt
Vortex
Corner
Vortex
x
c
z
T_0 = 25EC
Dimensionless Length
Deborah Number
0
2
4
6
0
2
4
6

Figure 7

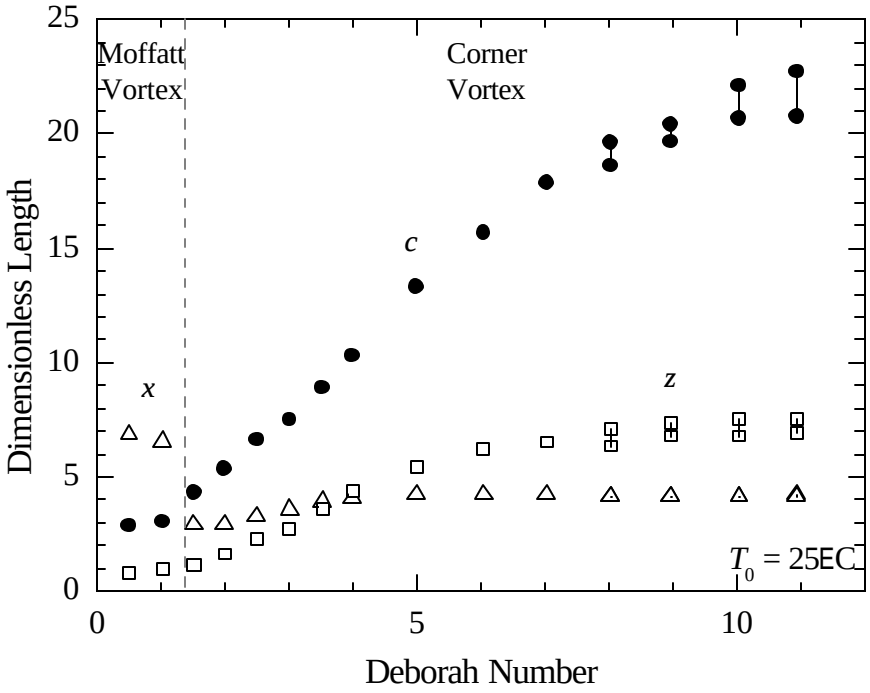
Moffatt
Vortex
Corner
Vortex
c
x
z
T_0 = 25EC
Dimensionless Length
Deborah Number
0
5
10
15
20
25
0
5
10

Figure 8

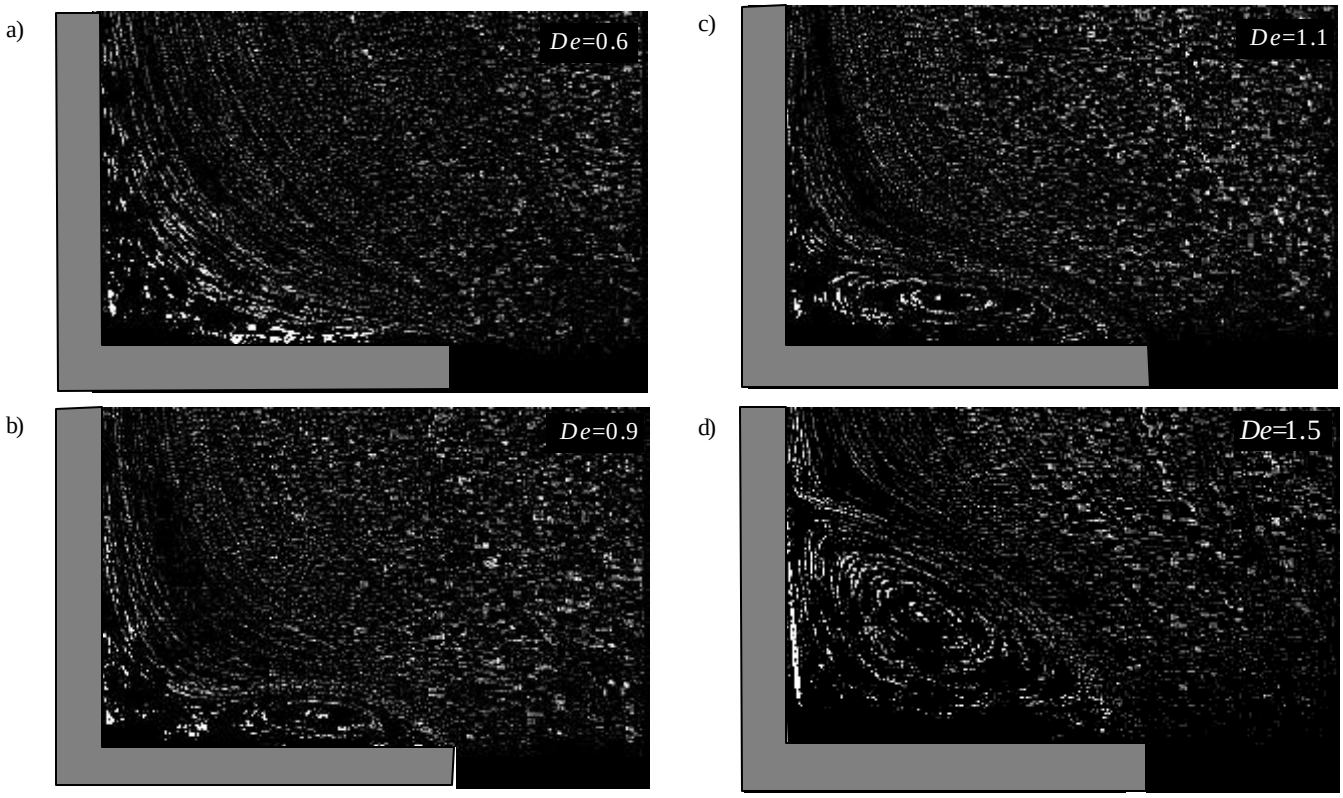

Figure 9

a)

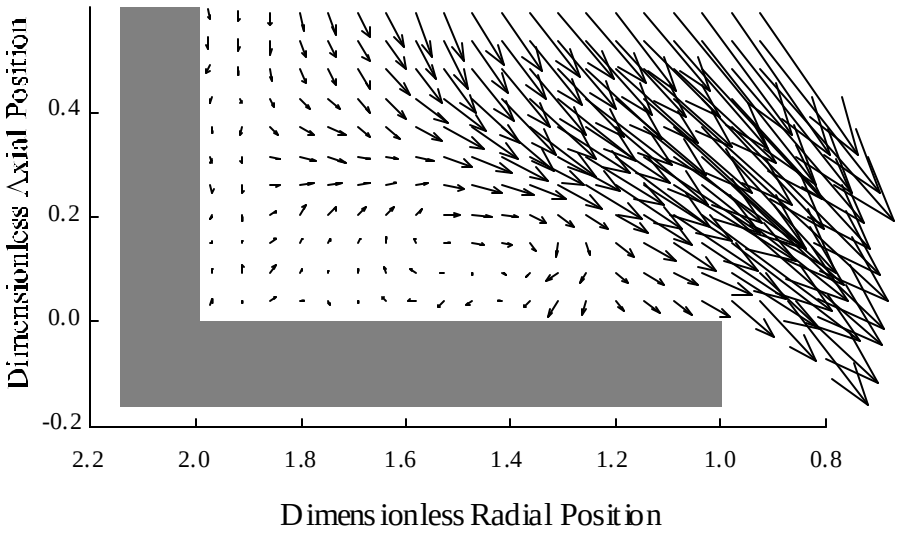
Dimensionless Axial Position
0.4
0.2
0.0
-0.2
2.2
2.0
1.8
1.6
1.4
1.2
1.0
0.8
Dimensionless Radial Position

b)

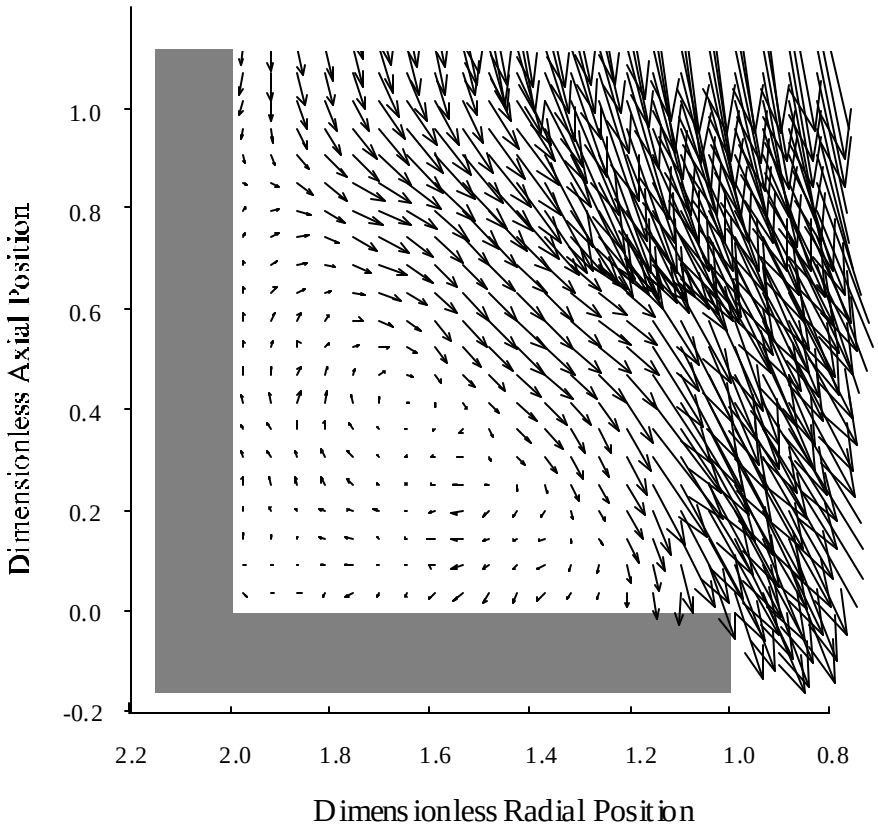
Dimensionless Axial Position
1.0
0.8
0.6
0.4
0.2
0.0
-0.2
2.2
2.0
1.8
1.6
1.4
1.2
1.0
0.8
Dimensionless Radial Position

Figure 10

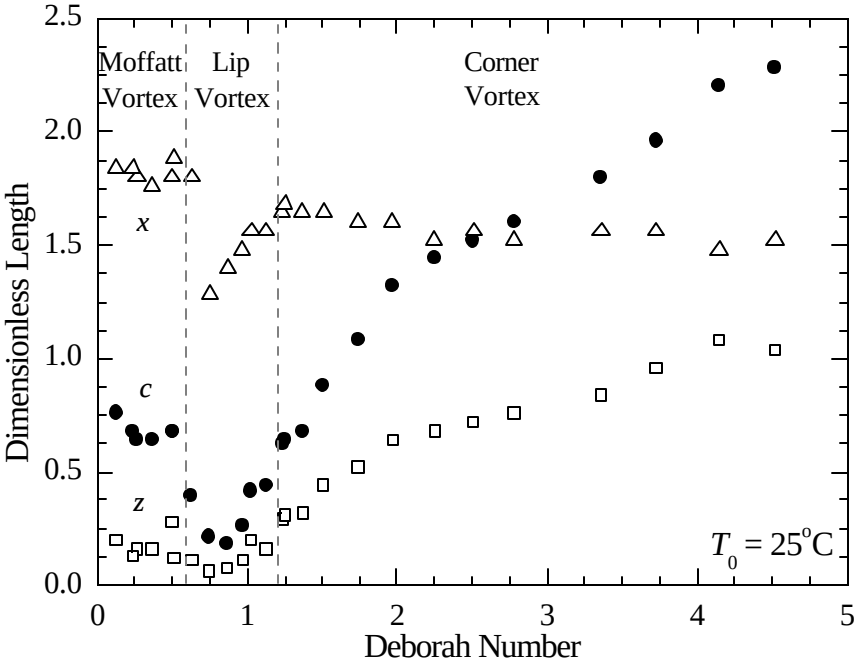
Moffatt Vortex
Lip Vortex
Corner Vortex
x
c
z
T_0 = 25°C
Dimensionless Length
Deborah Number
0.0
0.5
1.0
1.5
2.0
2.5
0
1
2
3
4
5

Figure 11

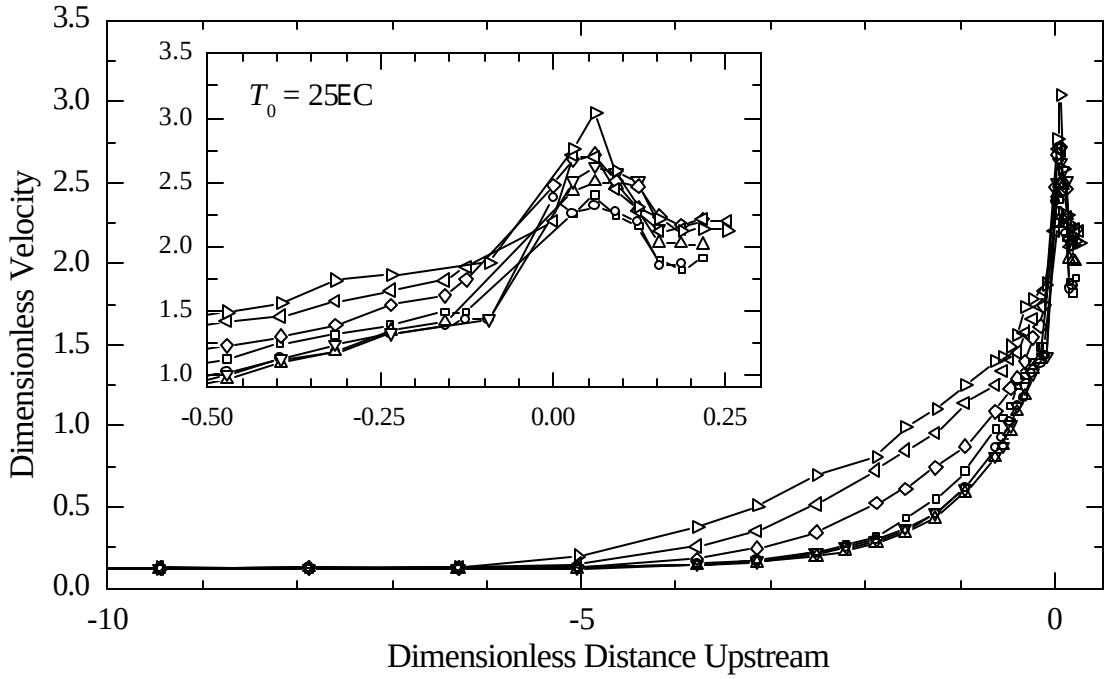
3.5
3.0
2.5
2.0
1.5
1.0
0.5
0.0
Dimensionless Velocity
-10
-5
0
Dimensionless Distance Upstream
T_0 = 25EC
3.5
3.0
2.5
2.0
1.5
1.0
-0.50
-0.25
0.00
0.25

Figure 12

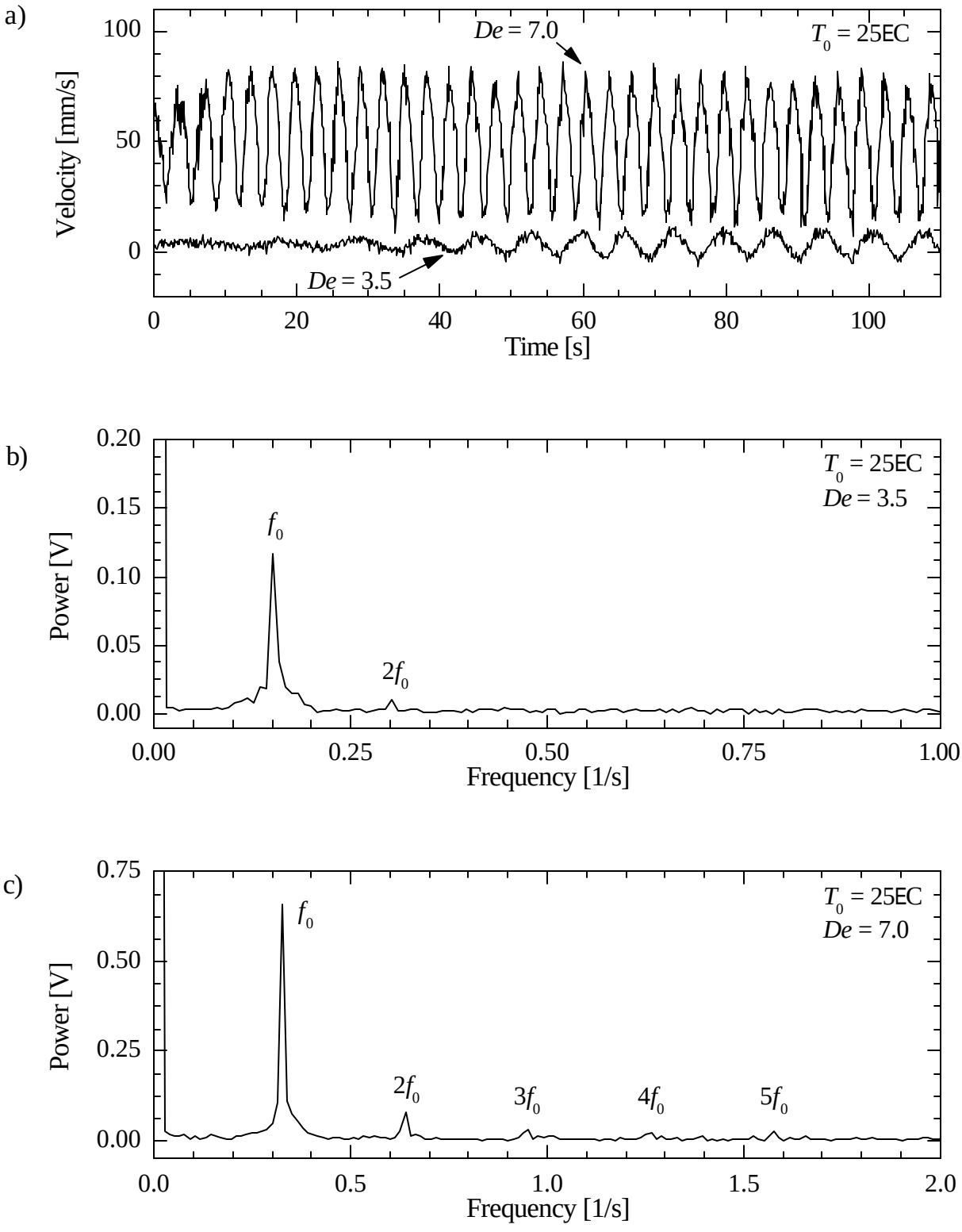
a)
100
50
0
Velocity [mm/s]
De = 7.0
T0 = 25EC
De = 3.5
0
20
40
60
80
100
Time [s]
b)
0.20
0.15
0.10
0.05
0.00
Power [V]
T0 = 25EC
De = 3.5
f0
2f0
0.00
0.25
0.50
0.75
1.00
Frequency [1/s]
c)
0.75
0.50
0.25
0.00
Power [V]
T0 = 25EC
De = 7.0
f0
2f0
3f0
4f0
5f0
0.0
0.5
1.0
1.5
2.0
Frequency [1/s]

Figure 13

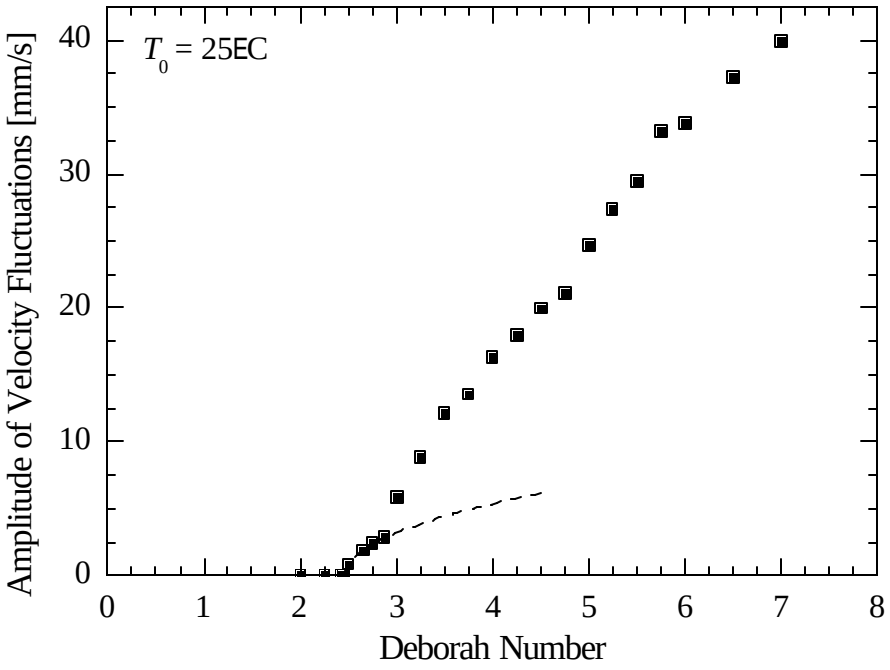
T_0 = 25EC
Amplitude of Velocity Fluctuations [mm/s]
Deborah Number
0
10
20
30
40
0
1
2
3
4
5
6
7
8

Figure 14

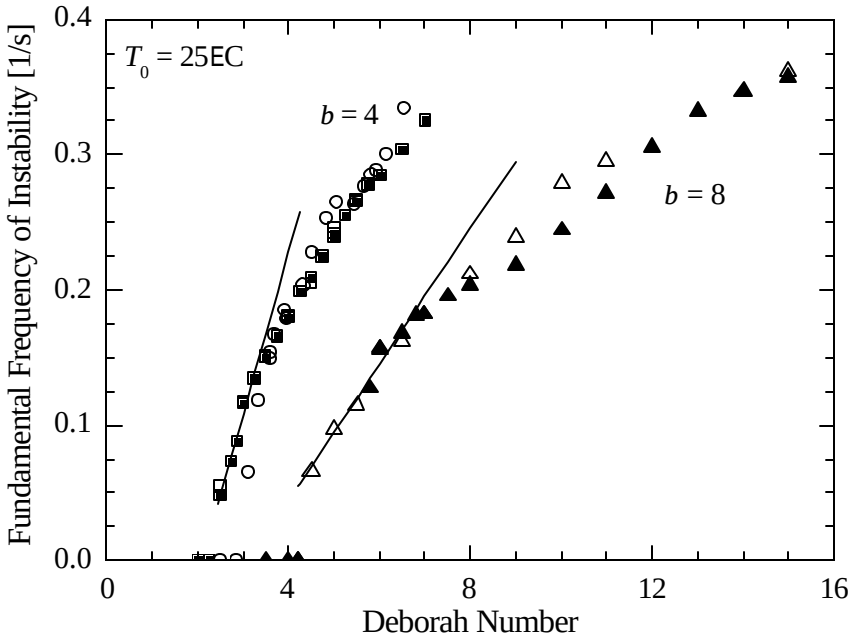
0.4
0.3
0.2
0.1
0.0
T_0 = 25EC
b = 4
b = 8
Fundamental Frequency of Instability [1/s]
0
4
8
12
16
Deborah Number

Figure 15

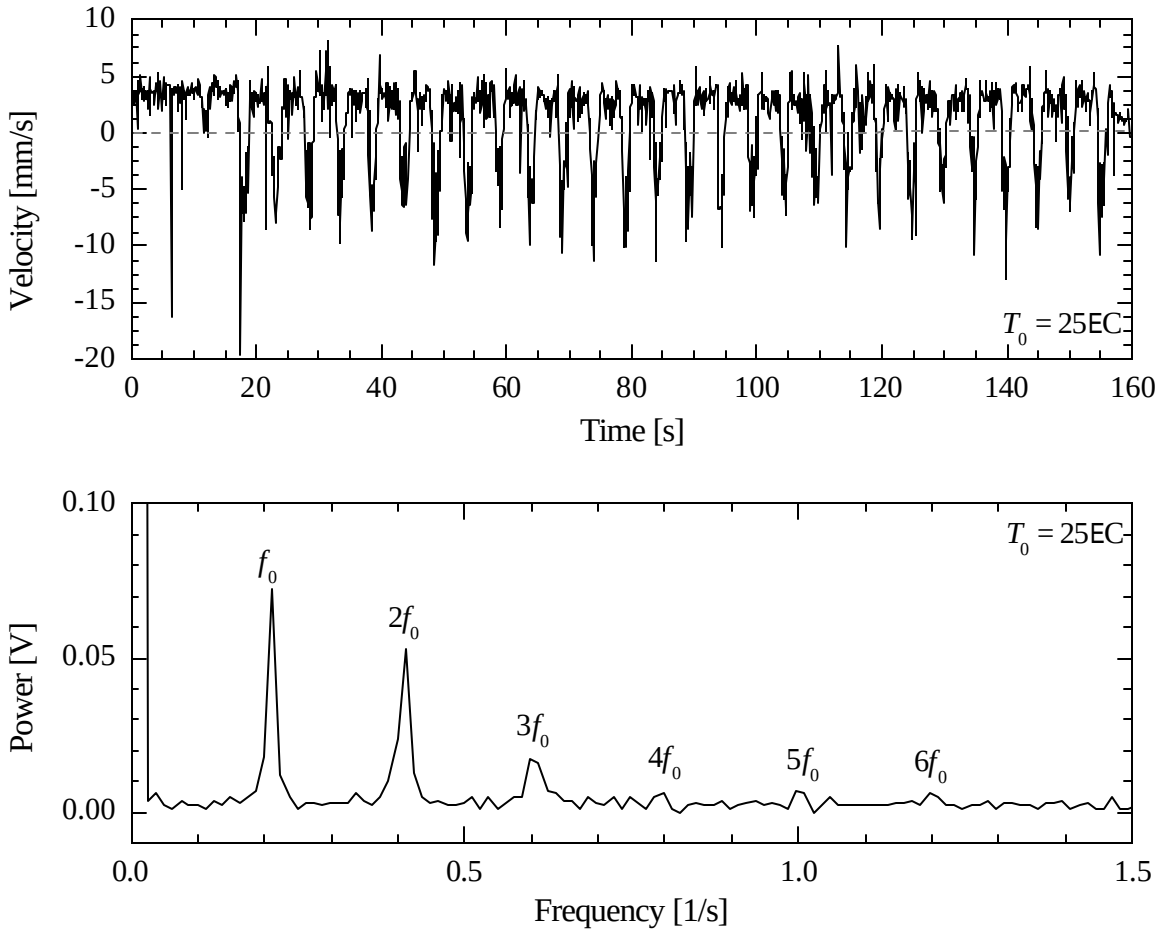
Velocity [mm/s]
Time [s]
T_0 = 25EC
Power [V]
Frequency [1/s]
f_0
$2f_0$
$3f_0$
$4f_0$
$5f_0$
$6f_0$

Figure 16

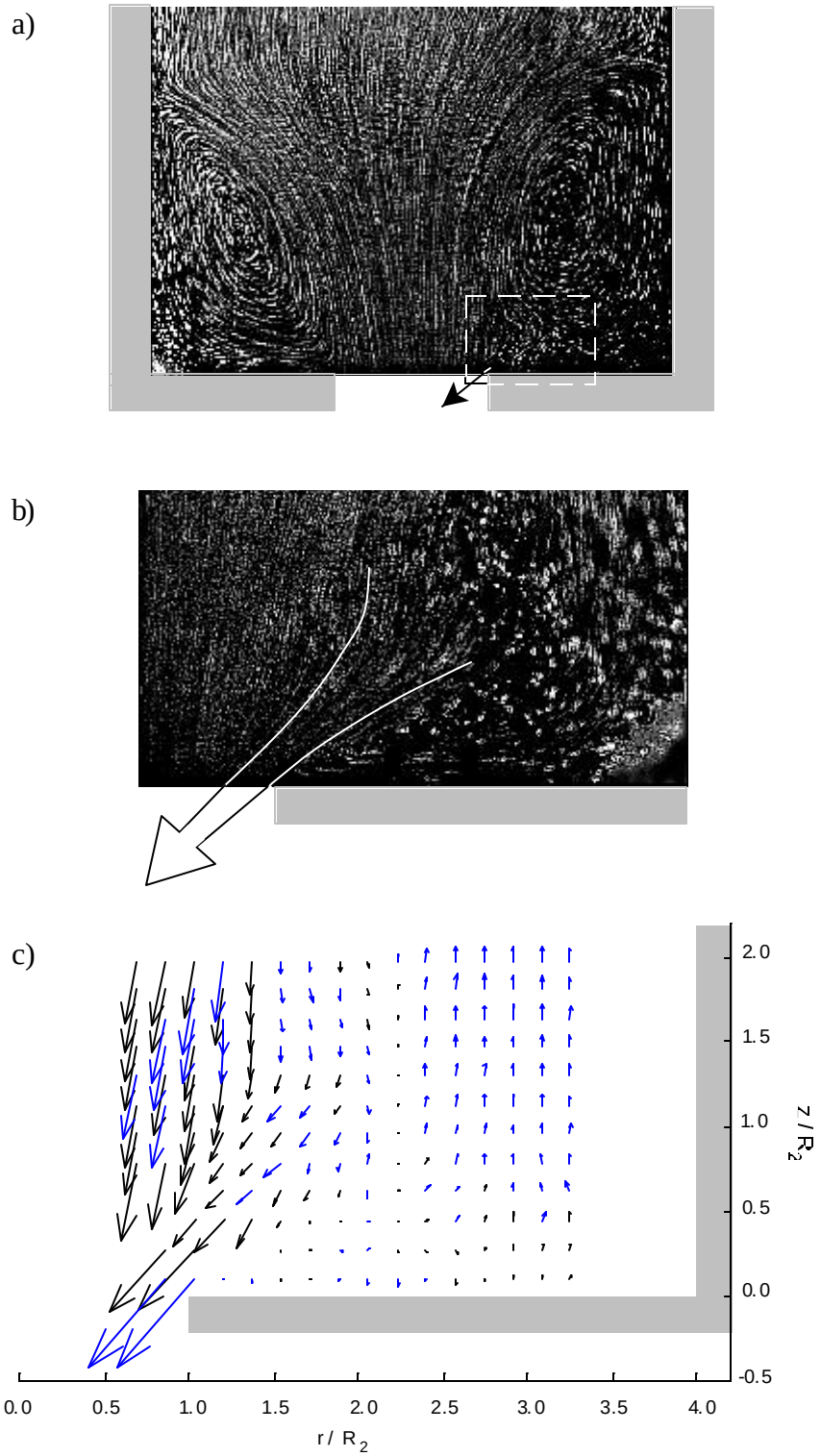

Figure 17

a)

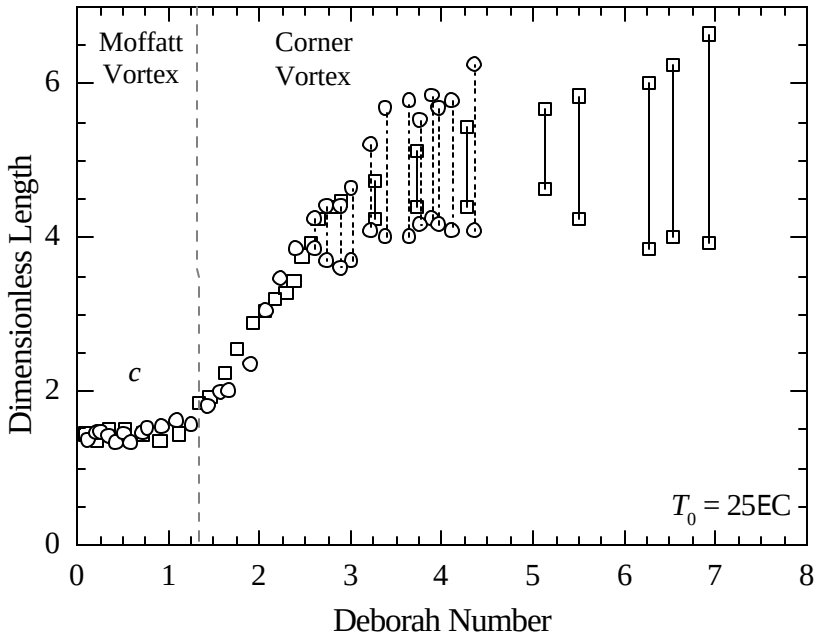
Moffatt
Vortex
Corner
Vortex
c
Dimensionless Length
Deborah Number
T_0 = 25EC
0
2
4
6
0
1
2
3
4
5
6
7
8

b)

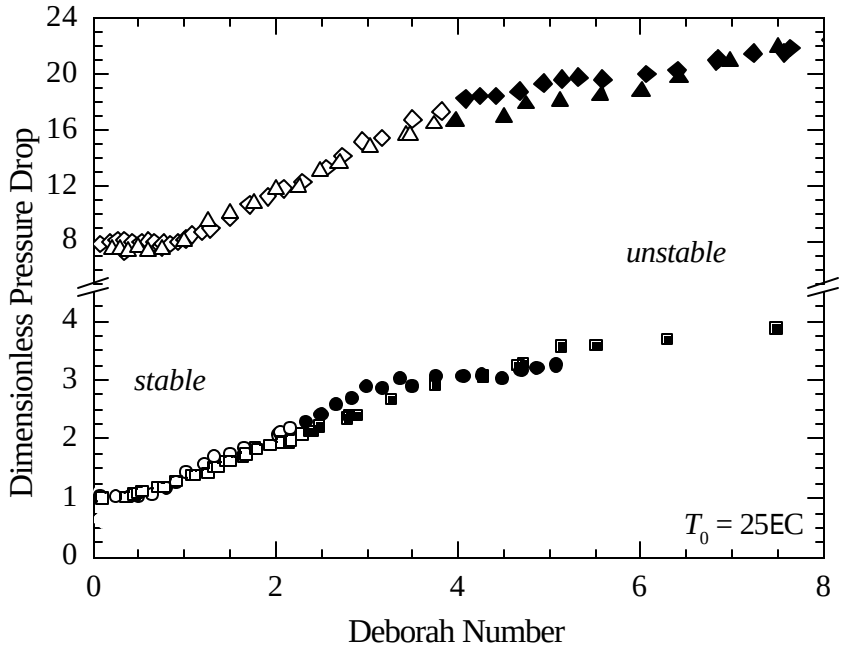
unstable
stable
Dimensionless Pressure Drop
Deborah Number
T_0 = 25EC
0
1
2
3
4
8
12
16
20
24
0
2
4
6
8

Figure 18

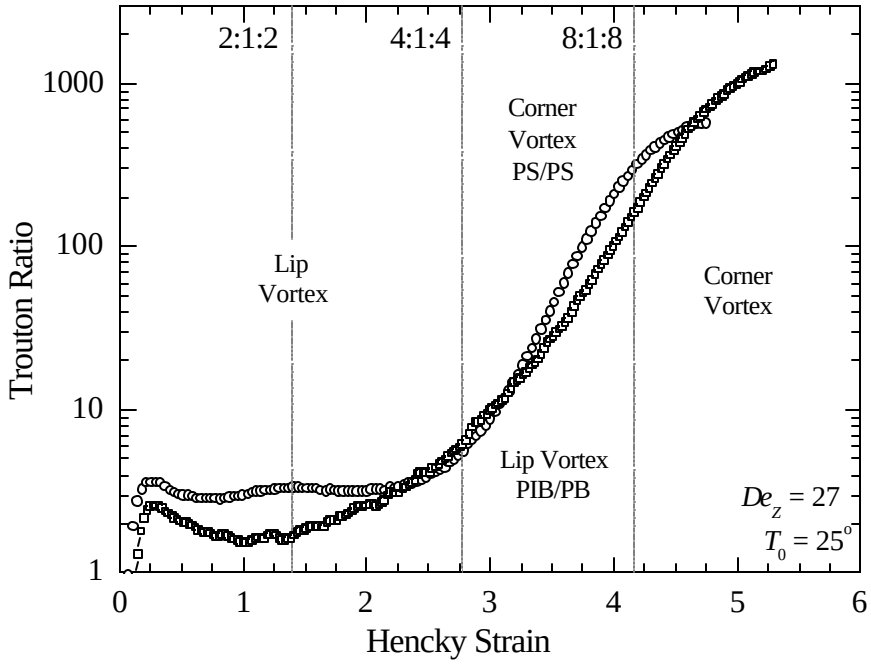
2:1:2
4:1:4
8:1:8
Corner
Vortex
PS/PS
Lip
Vortex
Corner
Vortex
Lip Vortex
PIB/PB
De_Z = 27
T_0 = 25°
Trouton Ratio
Hencky Strain
1000
100
10
1
0
1
2
3
4
5
6

Figure 19

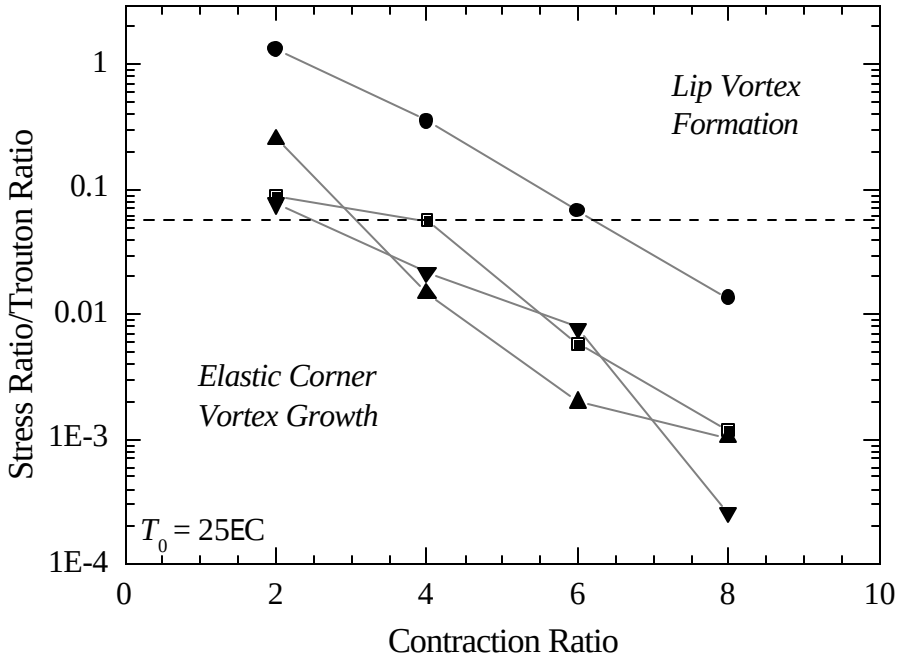
Stress Ratio/Trouton Ratio
1
0.1
0.01
1E-3
1E-4
0
2
4
6
8
10
Contraction Ratio
Lip Vortex
Formation
Elastic Corner
Vortex Growth
T0 = 25EC

Figure 20